PHANTOM-BASED REPEATABILITY IN HIGHER ORDER dMRI METRICS

KEEPING IT CONSISTENT: ASSESSING MEASUREMENT REPEATABILITY OF A NOVEL ANISOTROPIC PHANTOM FOR HIGHER ORDER DIFFUSION TENSOR MRI SEQUENCES

By LAUREN STEPHENS, B. Eng

A Thesis Submitted to the School of Graduate Studies in Partial Fulfillment of the Requirements for the Degree Master of Applied Science

McMaster University

MASTER OF APPLIED SCIENCE (2025)

Hamilton, Ontario, Canada (Biomedical Engineering)

TITLE:	Keeping It Consistent: Assessing Measurement Repeatability of a Novel Anisotropic Phantom for Higher Order Diffusion Tensor MRI Sequences
AUTHOR:	Lauren Stephens B.Eng (Electrical and Biomedical Engineering), McMaster University, Hamilton, Canada
SUPERVISOR:	Dr. Michael D. Noseworthy
NUMBER OF PAGES:	xiv, 99

Lay Abstract

Diffusion MRI is a non-invasive imaging technique that maps how water molecules move through tissue, offering insight into brain structure and health. It is especially valuable for detecting conditions like stroke, brain injury, and neurodegenerative disease. While newer diffusion models can capture more complex tissue features, they are also more prone to variation, raising concerns about how consistently they perform.

This thesis investigates the repeatability of advanced diffusion MRI methods using an object that simulates brain-like fibre structures, called a phantom. The phantom was scanned 11 times using various imaging protocols, including both standard and higher-order techniques. Results showed that conventional diffusion measurements were highly consistent, while more advanced metrics varied depending on the fibre complexity and scan type. These findings highlight which methods are most stable and help inform quality assurance practices in medical imaging, supporting more reliable use of advanced diffusion MRI in both research and clinical settings.

Abstract

Diffusion MRI (dMRI) provides valuable insight into tissue microstructure for clinical and research applications. Traditional diffusion tensor imaging (DTI) models diffusion as a Gaussian process, which limits its accuracy in regions with complex fibre configurations (such as crossing or bifurcating tracts). Higher-order models, including diffusion kurtosis imaging (DKI) and constrained spherical deconvolution (CSD), address these limitations by capturing non-Gaussian diffusion behaviour or resolving multiple fibre orientations within a voxel. Despite their theoretical advantages, these models are more sensitive to noise and acquisition variability, raising concerns about repeatability. Currently, there is no standardized method to perform quality assurance (QA) on dMRI data, and there are limited studies measuring the repeatability of higher-order tensor metrics.

This thesis evaluates the repeatability of higher-order dMRI metrics using a novel anisotropic phantom developed by PreOperative Performance (Toronto, ON). The phantom contains fibre modules with controlled geometries (linear, branching, and crossing bundles) designed to mimic white matter tract architecture. Six diverse regions of interest (ROIs) were assessed across 11 independent imaging sessions using DTI, high angular resolution diffusion imaging (HARDI), and DKI protocols.

Repeatability was quantified using coefficient of variation (CoV) and intraclass correlation coefficient (ICC).

DTI-derived metrics, including fractional anisotropy (FA), mean diffusivity (MD), axial diffusivity (AD), and radial diffusivity (RD), exhibited excellent repeatability (CoV $< 10\%$, ICC > 0.9). HARDI acquisitions (60- and 90-direction) yielded slightly improved repeatability over DTI. DKI metrics, including mean kurtosis (MK), axial kurtosis (AK), radial kurtosis (RK), and kurtosis fractional anisotropy (KFA), showed greater variability, particularly in ROIs with fibre crossings. Generalized fractional anisotropy (GFA), derived from CSD, demonstrated increasing ICCs with higher angular resolution: 0.66 (DTI), 0.80 (HARDI-60), and 0.85 (HARDI-90). These findings support the phantom's utility for repeatability testing and contribute toward developing QA standards for advanced dMRI models.

To my parents

Acknowledgements

First and foremost, I would like to thank my supervisor, Dr. Michael Noseworthy, for his mentorship and expertise. The undergraduate courses I took with him were foundational in shaping my interest in MRI and electrical engineering, and I am so grateful to have been taught by someone with so much passion and knowledge. His thoughtful feedback and steady guidance throughout this project has pushed me to think critically and grow as a researcher, something I will carry with me well beyond this degree.

I would also like to thank the staff members at the Imaging Research Centre at St. Joe's who helped make this research a reality. Thank you to Norm Konyer for his technical support and willingness to answer any of my questions. Also a huge thank you to the MRI technologists (Shannon, Suzanne, and Julie) for taking the time to train me on using the MRI. My many hours of scanning would not have been possible without their patience.

I am especially grateful to Fergal Kerins at PreOperative Performance for his generosity and support throughout this project. From providing access to the phantom to offering valuable insights along the way, I am grateful to have this collaboration opportunity with someone so knowledgeable and engaged.

To my lab partners in Dr. Noseworthy's lab, thank you for being such a supportive

and kind group of people. I've learned so much from each of you and feel very lucky to have been part of a lab environment that was so welcoming and encouraging. I always look forward to our Thursday morning lab meetings, which kept me on track and motivated.

To my family and friends, thank you for cheering me on through every stage of my education. Special thanks to the Broadway girls for always being there for a late night kitchen chat or innertube waterpolo game–your friendship has meant so much throughout the years. To Akram, thank you for being my #1 supporter and keeping me fed, caffeinated, and sane throughout the writing process. Your unconditional love and support means the world to me. To my mom Jacqueline and my dad Paul, thank you for the many ways you've supported me, both big and small. I'm so lucky to have parents who encouraged me every step of the way and always reminded me that I could do anything I set my mind to.

Table of Contents

List of Figures

List of Tables

Abbreviations

ADC	Apparent diffusion coefficient
AD	Axial diffusivity
AK	Axial kurtosis
ANOVA	Analysis of variance
CoV	Coefficient of variation
CSD	Constrained spherical deconvolution
DICOM	Digital Imaging and Communications in Medicine
DIPY	Diffusion Imaging in Python
dMRI	Diffusion magnetic resonance imaging
DTI	Diffusion tensor imaging
DKI	Diffusion kurtosis imaging
DWI	Diffusion weighted imaging
FA	Fractional anisotropy
FGE	Fast gradient echo
FLIRT	FMRIB's Linear Image Registration Tool
FMRIB	Functional Magnetic Resonance Imaging of the Brain

fODF	Fibre orientation distribution function
FSL	FMRIB Software Library
FSPGR	Fast spoiled gradient echo
GFA	Generalized fractional anisotropy
GRE	Gradient recalled echo
HARDI	High angular resolution diffusion imaging
ICC	Intraclass correlation coefficient
MD	Mean diffusivity
MK	Mean kurtosis
MP-PCA	Marchenko–Pastur Principal Component Analysis
NIFTI	Neuroimaging Informatics Technology Initiative
NMR	Nuclear magnetic resonance
PGSE	Pulsed gradient spin echo
PVA	Polyvinyl alcohol
PVP	Polyvinylpyrrolidone
QA	Quality assurance
RD	Radial diffusivity
RF	Radiofrequency
RK	Radial kurtosis
ROI	Region of interest
SD	Standard deviation
SH	Spherical harmonic
SNR	Signal-to-noise ratio

SS-EPI	Single-shot echo planar imaging
TE	Echo time
TR	Repetition time
UHMWPE	Ultra high molecular weight polyethylene

Chapter 1

Introduction

Diffusion magnetic resonance imaging (dMRI) is a non-invasive imaging technique that probes the microscopic movement of water molecules in biological tissues. Routine MRI protocols may include a T1-weighted or T2-weighted scan, where image contrast arises from differences in longitudinal and transverse relaxation times, respectively. In comparison, dMRI generates contrast weighted to the diffusivity of water. Since water diffusion is influenced by structural barriers such as cell membranes, axonal fibres, and extracellular matrix components, dMRI can reveal important features and pathological changes that are not detectable with standard anatomical imaging. This makes dMRI particularly valuable in neuroimaging, where it is frequently employed to assess conditions such as stroke, traumatic brain injury, and neurodegenerative disease [1–5]. dMRI allows for the assessment of diffusion properties through quantitative scalar metrics such as apparent diffusion coefficient (ADC), fractional anisotropy (FA), and mean diffusivity (MD). These derived scalars can help provide an objective comparison of results between patients or time points.

Despite its utility, dMRI is susceptible to issues with standardization and reproducibility, particularly in areas with complex diffusion geometry. In the brain, white matter tracts can cross, fan, and branch, which results in differently oriented fibre bundles being present in the same voxel. Traditional dMRI-derived metrics assume one principal diffusion direction, which leads to inaccuracies at these locations (often called the "crossing-fibre problem"). Estimates of the percentage of white matter voxels affected by crossing-fibre effects range from 33% to 90% [6–8]. Compounding the issue, it has been widely established that dMRI signal intensity can differ even when imaging the same subject on the same scanner within a short time period, due to slow, progressive changes in the MRI baseline signal over time (a phenomenon called "scanner drift"). Potential origins of scanner drift in dMRI data include B_0 field instability, flip angle drift, or even heating of the gradient subsystems [9]. In addition to intra-scanner variability, several studies have demonstrated substantial inter-vendor differences in diffusion measurements, even when using harmonized protocols [10, 11]. These vendor-level differences arise from variations in gradient hardware, pulse sequence design, and reconstruction algorithms.

To overcome the limitations of conventional dMRI modelling in regions of complex fibre architecture, several advanced modelling techniques have been developed. Higher-order diffusion models, such as diffusion kurtosis imaging (DKI), extend the diffusion tensor framework to capture non-Gaussian diffusion behaviour [12]. DKI introduces a fourth-rank tensor to quantify the degree of kurtosis, or deviation from

Gaussian diffusion, which is particularly relevant in regions with cellular heterogeneity or restricted diffusion. Meanwhile, orientation-resolved techniques such as constrained spherical deconvolution (CSD) allow for modelling of multiple fibre populations within a single voxel by estimating a fibre orientation distribution function (fODF) [13]. These techniques require more extensive data acquisition protocols with a greater number of diffusion directions and higher b-values. While these models provide a more accurate characterization of complex fibre configurations, they are also more sensitive to noise and scanner instability, which raises questions about their reproducibility.

1.1 Motivation and Rationale

To address this gap, a novel anisotropic diffusion phantom developed by PreOperative Performance (Toronto, ON) has been introduced. This phantom is designed to better emulate the scale and structure of brain tissue, including the directional and restricted diffusion characteristics of white matter tracts. Preliminary studies have demonstrated its potential for evaluating standard rank-2 tensor metrics (specifically FA and MD) across multiple scanner platforms [14]. However, further validation is needed to determine its repeatability for higher-order diffusion models and metrics.

1.2 Research Objectives and Hypothesis

The goal of this work was to evaluate the repeatability of advanced higher-order tensor diffusion MRI metrics using a novel anisotropic phantom. Specifically, this research aimed to:

1. Assess literature to draw conclusions on the consistency of the PreOperative Performance phantom relative to other available phantoms.

2. Provide a baseline consistency by assessing the repeatability of conventional rank-2 tensor diffusion metrics, including fractional anisotropy, mean diffusivity, radial diffusivity (RD), and axial diffusivity (AD).

3. Evaluate the repeatability of rank-4 diffusion kurtosis parameters, including kurtosis fractional anisotropy (KFA), mean kurtosis (MK), axial kurtosis (AK), and radial kurtosis (RK).

4. Explore alternative methods of modelling diffusion data that incorporate multiple primary fibre directions and evaluate their suitability and repeatability for resolving crossing-fibre voxels.

The central hypothesis of this work was that the PreOperative Performance phantom is capable of producing consistent and repeatable higher-order dMRI metrics across repeated imaging sessions. Specifically, it was hypothesized that the phantom could support reliable measurements for both standard rank-2 tensor metrics and higher-rank tensor metrics. It was also hypothesized that diffusion models which incorporate multiple primary fibre directions would resolve crossing fibre locations with less local variability.

This thesis aimed to contribute to the body of research focused on quality assurance (QA) of MRI. The work expands on previous studies investigating the PreOperative Performance phantom by systematically assessing its variability with DKI and CSD modelling. This research was among the first to evaluate the repeatability of advanced dMRI metrics using a physical phantom designed specifically for

anisotropic diffusion. These results will help inform the suitability of the phantom for these scanning protocols, leading to a better understanding of MRI scanner performance, especially during longitudinal dMRI studies on the same patient. The work also supports the continued development of QA tools and contributes to the better implementation of advanced dMRI techniques.

1.3 Thesis Organization

The thesis is organized as follows:

Chapter 2 establishes a background on dMRI, including the theory and techniques used in this research.

Chapter 3 provides a brief literature review on diffusion phantoms, focusing on compiling results from various multi-centre phantom studies.

Chapter 4 outlines the materials and methods of the study, including the scanning protocol, diffusion modelling, and statistical analysis being employed.

Chapter 5 presents the performance and repeatability results for the various scanning and modelling techniques.

Chapter 6 concludes the thesis by summarizing the results, identifying limitations, and proposing next steps.

Chapter 2

Background on MRI Diffusion

2.1 Introduction to Diffusion Imaging

Quantitative measurements of diffusion first began in nuclear magnetic resonance (NMR), prior to MRI being invented. Diffusion in NMR was accounted for in Hahn's paper on the spin echo phenomenon [15], Carr and Purcell's work on measuring signal loss due to diffusion [16], and Torrey's mathematical incorporation of diffusion into Bloch equations [17]. Throughout the late 1970s and early 1980s, diffusion NMR was studied extensively and applied to a wide range of biological samples. In 1982, Mansfield and Morris suggested diffusion imaging using MRI could be implemented by combining Fourier NMR and magnetic pulse gradients. This proposal laid the groundwork for diffusion-sensitive MRI techniques, leading to the first human diffusion-weighted images published in 1986 by Le Bihan et al [18].

2.1.1 Molecular Diffusion

Diffusion is the movement of molecules or ions in a system from a region of high concentration to a region of low concentration. This is an important principle for numerous physiological functions, including gas exchange in the lungs, the distribution of nutrients in the bloodstream, the exchange of oxygen and carbon dioxide in the microvasculature, and the transmission of signals between nerve cells. Brownian motion, first described by Robert Brown in 1827, drives diffusion through the constant random thermal motion of molecules [19]. In a free homogeneous environment, water molecules diffuse uniformly in all directions, obeying a Gaussian (i.e. normal) distribution, according to Einstein's equation:

$$\langle r^2 \rangle = 2NDt \tag{2.1.1}$$

where r^2 is the mean squared displacement, t is the observation time, N is the dimensionality of the observation space, and D is the diffusion coefficient [20]. This equation characterizes the random behaviour of the molecules by stating that the squared displacement is directly proportional to the observation time.

Isotropic diffusion occurs when molecules are free to diffuse equally in all directions. In contrast, anisotropy occurs when there is unequal directional diffusivity, caused by restricted diffusion (Figure 2.1). In biological tissues, diffusion is not entirely free; instead, it is influenced by structural barriers such as cell membranes, fibres, and macromolecules. In the brain, isotropic diffusion is observed in ventricles filled with cerebrospinal fluid, whereas anisotropic diffusion is observed along white matter tracts, since diffusion is primarily parallel along the fibre's long axis

and limited in the tangential direction.

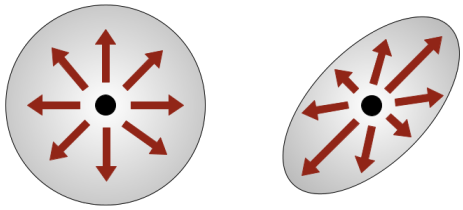

Figure 2.1: Schematic illustration of isotropic (left) and anisotropic (right) diffusion.

2.1.2 Image Acquisition Theory

In the context of MRI, diffusion is measured by the application of magnetic field gradients, which makes the resulting images sensitive to the motion of water molecules. By applying a linear magnetic field gradient, the precessional frequency of the protons will vary spatially, according to the Larmor equation:

$$\omega = \gamma B_0 \tag{2.1.2}$$

where ω is the precessional frequency of the protons (in MHz), B_0 is the strength of the external magnetic field (in Tesla, T), and γ is the gyromagnetic ratio (in MHz/T). The applied gradient gives the protons a position-dependent precessional frequency, which induces a phase shift. By applying a second gradient pulse with the same magnitude and polarity, the phase shift is reversed, refocusing the protons. In between the two pulses, the protons are free to diffuse and move along the gradient. Thus, the sum of the applied gradients do not "cancel out", and there will be a net phase change dependent on the displacement of the proton.

The MRI instrumentation measures the sum of the signals within each voxel, so

the strongest signal is measured when there is a coherent frequency and phase of the protons. In an isotropic environment, molecules have unrestricted diffusion, meaning they will have a greater net displacement and a less coherent signal. Conversely, an anisotropic environment will have less displacement and produce a stronger signal. From the signal intensity, the diffusion coefficient of the protons can be estimated.

In practice, diffusion MRI sequences typically use a pulsed gradient spin-echo (PGSE) sequence, first proposed by Stejskal and Tanner [21]. Here, a 90-degree radiofrequency (RF) pulse creates an initial signal by exciting the water molecules' magnetic moment into the transverse plane. Next, the diffusion-sensitizing gradient is applied, which creates the position-dependent precessional frequency. A 180-degree RF pulse is emitted, called the refocusing pulse, which inverts the spin phase. Another equal magnitude and duration diffusion-sensitizing gradient is applied, which reverses the loss of coherence (Figure 2.2). In diffusion sequences, it is important to note that both the diffusion-encoding gradients and spatial-encoding gradients are created from the same gradient hardware. As such, diffusion-encoding gradients are not applied during RF pulses or data acquisition.

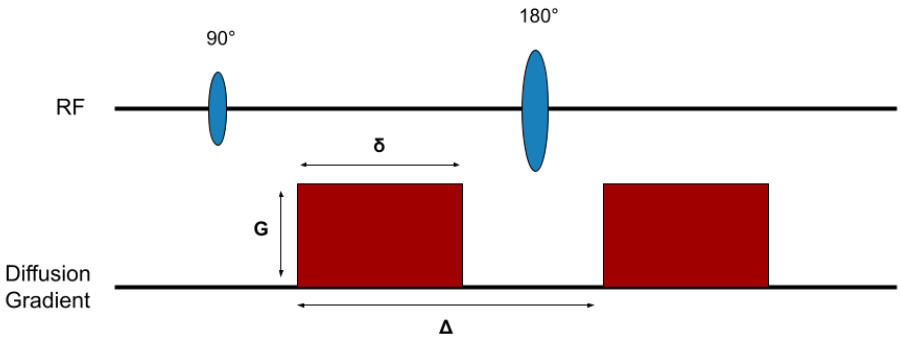

Figure 2.2: Diagram of key elements in the PGSE sequence.

The attenuation of the signal is affected by γ, the gyromagnetic ratio; G, the amplitude of the diffusion-encoding gradient pulses; δ, the duration of the gradient pulse; and Δ, the temporal separation between the rising edge of the two gradient pulses (i.e. the diffusion time). The degree of diffusion weighting applied by the gradient is combined into a "b-value" scalar factor (measured in units of seconds/mm^2), given by the Stejskal-Tanner equation [21]:

$$b = \gamma^2 G^2 \delta^2 (\Delta - \frac{\delta}{3}) \tag{2.1.3}$$

A high b-value (e.g. $b > 2000$ s/mm^2) uses long, large-amplitude gradients with a long inter-gradient time, making them highly sensitive to diffusion and useful to measure slow-moving protons (e.g. those that are electrostatically bound to macromolecules). Intermediate b-values (e.g. b between 50 and 1000 s/mm^2) represent freely diffusing water protons, while small b-values (e.g. $b < 50$ s/mm^2) are only sensitive to fast-moving protons, such as microvascular blood flow (i.e. perfusion).

The routine quantification of diffusion is done by measuring the signal amplitudes at two different b-values. The relationship between signal and the diffusion coefficient, D, is a single exponential relationship, with the coupling factor being the b-value. The attenuation of the signal is given as:

$$S_b = S_0 e^{-b \cdot D} \tag{2.1.4}$$

where S_0 is the signal with $b = 0$, which can be achieved by setting $G = 0$. S_b is the signal at some value of b, achieved by setting G to the appropriate value. Since S_0, S_b, and b are known, the above equation can be rearranged to calculate D from the

measured data.

2.2 Modelling Techniques in Diffusion MRI

2.2.1 Diffusion Weighted Imaging

Diffusion Weighted Imaging (DWI) is the foundational technique upon which advanced dMRI methods are built. In its simplest form, DWI acquires imaging along three orthogonal directions, yielding diffusion coefficients (D_{xx}, D_{yy}, and D_{zz}). To capture the overall diffusion across the probed directions, the ADC is calculated as:

$$ADC = \frac{D_{xx} + D_{yy} + D_{zz}}{3} \tag{2.2.1}$$

ADC is sometimes used interchangeably with the diffusion coefficient D, leading to confusion. D represents the true physical rate of diffusion due to thermal motion. It is influenced by factors like temperature or the viscosity of the surrounding medium. Diffusion measured through MRI is considered "apparent" because it reflects the rate of diffusion coupled with restriction imposed by structures like cell membranes and extracellular matrix components [22]. A major limitation of DWI is that it does not capture information regarding the direction of diffusion. DWI-metrics like ADC only provide a single scalar value that measures the average magnitude of diffusion in the gradient directions.

In the brain, DWI is a well-established method for diagnosing, evaluating, and managing acute ischemic stroke, making it a routine tool within the clinical setting. Moseley et al. were the first to show restricted diffusion in ischemic regions of the brain

using DWI of animal models [23]. The physiological cause of this restricted diffusion is not fully elucidated, however, the breakdown of cellular energy metabolism and the resultant failure of the sodium-potassium (Na+/K+) ATPase pumps appear to contribute [24]. As a result, sodium ions accumulate inside cells, causing water to shift from the extracellular space into the intracellular space, leading to cytotoxic edema within minutes after stroke onset. This swelling of cells reduces the mobility of water molecules, which is detected as restricted diffusion on DWI. This leads to a drop in ADC, often visible through DWI scans before structural changes become visible on T1- or T2-weighted scans [25].

PROPELLER Acquisition

The typical approach to dMRI acquisition is through the use of echoplanar imaging (EPI), which fills the raw data space (i.e. k-space) in a single shot (SS) [26]. The imaging gradients in an EPI sequence fill k-space in a raster fashion by rapidly oscillating, allowing a single slice (matrix size of 64x64) acquisition on the order of 65-80ms, depending on vendor and magnetic field gradient specifications. During SS-EPI, the entire k-space is traversed following an RF excitation using a rapid train of gradient echoes, commonly in a "zig-zag" trajectory (Figure 2.3). This design minimizes acquisition time, but extends the duration of the readout window where k-space is collected. Off-resonance effects from field inhomogeneities, eddy currents, and susceptibility gradients can cause geometric distortion and spatial blurring. Additionally, any patient motion during the readout window immediately corrupts the whole image, resulting in severe artifacts.

One variation of this scheme is the Periodically Rotated Overlapping Parallel Lines

with Enhanced Reconstruction (PROPELLER) technique, which is a non-Cartesian k-space sampling strategy that has been adapted for DWI to mitigate artifacts commonly associated with SS-EPI-based acquisitions [27]. In PROPELLER DWI, data is collected as a series of rotating, overlapping rectangular "blades", which sample k-space centred around the origin (Figure 2.3). The shorter readout per blade reduces the time when off-resonance effects can accumulate, resulting in less distortion and improved image fidelity, especially in areas near air-tissue interfaces. The central region of k-space is oversampled, allowing for retrospective correction for motion. The PROPELLER acquisition scheme increases scan time, but provides a distortion-minimized diffusion image.

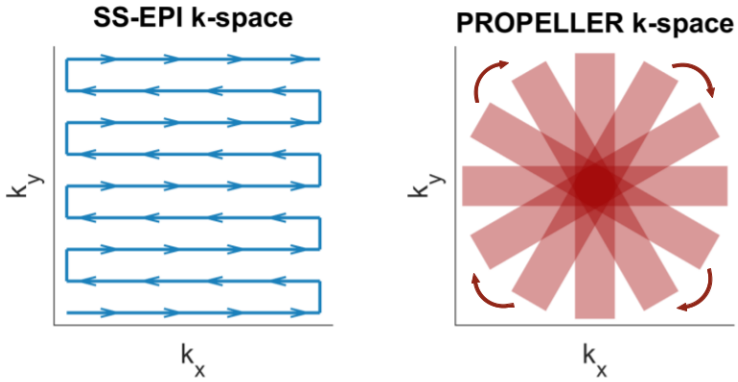

Figure 2.3: Comparison of k-space trajectories in SS-EPI and PROPELLER diffusion MRI acquisitions.

2.2.2 Diffusion Tensor Imaging

Diffusion tensor imaging (DTI) is an extension of DWI that models diffusion as a three-dimensional Gaussian distribution. It provides information on diffusion anisotropy

and directionality by representing diffusion as a second-order tensor, **D**:

$$\mathbf{D} = \begin{bmatrix} D_{xx} & D_{xy} & D_{xz} \\ D_{xy} & D_{yy} & D_{yz} \\ D_{xz} & D_{yz} & D_{zz} \end{bmatrix}$$

DTI was first introduced by Basser et al. in the mid-1990s, where they aimed to quantify anisotropy through scalar metrics and map diffusion directionality [28]. This provided the mathematical foundation for constructing the diffusion tensor and calculating fractional anisotropy and mean diffusivity. DTI is now widely adopted in both research and clinical settings, particularly in the study of white matter integrity [29, 30]. Clinically, DTI has found application in pre-surgical planning for tumour resection through tractography, where white matter pathways are reconstructed around the tumour to inform the surgical approach [31, 32].

As with DWI, DTI assumes water diffusion follows a Gaussian distribution. It represents diffusion with a single tensor per voxel, which gives one dominant diffusion direction, represented by the primary eigenvector of the diffusion tensor. These assumptions neglect the presence of multiple fibre populations or non-Gaussian diffusion behaviour, leading to potential mischaracterizations of diffusion properties.

Properties of the Diffusion Tensor

D is a symmetric positive semi-definite 3×3 matrix where each element, D_{ij} represents the diffusion coefficient along the i-th and j-th directions in 3D space. This second-rank tensor characterizes the directional dependence of diffusion, mapping a diffusion gradient vector to a corresponding diffusion-weighted signal. **D** is symmetric (since

the rate of diffusion from x to y is the same as from y to x), meaning there are six independent coefficients to solve for. As such, DTI images must be acquired along at least six non-collinear directions, in addition to $b = 0$ image. In clinical practice, more directions (typically 12-30) are often acquired to increase the signal-to-noise ratio (SNR) and improve the precision of the tensor estimation.

The Stejskal-Tanner equation (2.1.4) is generalized to the tensor form [28]:

$$S(b, \mathbf{g}) = S_0 e^{-b\mathbf{g}^\intercal \mathbf{D}\mathbf{g}} \tag{2.2.2}$$

where:

- $S(b, \mathbf{g})$ is the measured signal with diffusion gradient direction $\mathbf{g}$ and b-value b applied
- S_0 is the signal when $b = 0$
- b is the b-value
- $\mathbf{g}$ is the 3×1 column unit vector in the direction of the applied gradient
- $\mathbf{D}$ is the 3×3 diffusion tensor

Expanding $\mathbf{g}^\intercal \mathbf{D}\mathbf{g}$ gives:

$$\mathbf{g}^\intercal \mathbf{D}\mathbf{g} = D_{xx}g_x^2 + D_{yy}g_y^2 + D_{zz}g_z^2 + 2D_{xy}g_x g_y + 2D_{xz}g_x g_z + D_{yz}g_y g_z \tag{2.2.3}$$

Rearranging and taking the natural logarithm of Equation 2.2.2 gives the linear relationship between the log-signal and the tensor components:

$$\ln(\frac{S(b, \mathbf{g})}{S_0}) = -b(D_{xx}g_x^2 + D_{yy}g_y^2 + D_{zz}g_z^2 + 2D_{xy}g_x g_y + 2D_{xz}g_x g_z + 2D_{yz}g_y g_z) \tag{2.2.4}$$

Defining:

$$Y = \ln\left(\frac{S(b,\mathbf{g})}{S_0}\right)$$

$$\mathbf{X} = [g_x^2, g_y^2, g_z^2, 2g_xg_y, 2g_xg_z, 2g_yg_z]$$

$$\boldsymbol{\beta} = [D_{xx}, D_{yy}, D_{zz}, D_{xy}, D_{xz}, D_{yz}]^\intercal$$

We can express the system for each measurement as:

$$Y = -b\mathbf{X}\boldsymbol{\beta} \tag{2.2.5}$$

Acquiring multiple diffusion-weighted images with different $\mathbf{g}$ directions forms an overdetermined linear system, which can be solved for the tensor elements in $\boldsymbol{\beta}$ using least-squares fitting.

After computing $\mathbf{D}$, it is diagonalized:

$$\mathbf{D} = \mathbf{E}\boldsymbol{\Lambda}\mathbf{E}^\intercal \tag{2.2.6}$$

where $\boldsymbol{\Lambda}$ contains the eigenvalues and $\mathbf{E}$ contains the eigenvectors of the diffusion tensor:

$$\boldsymbol{\Lambda} = \begin{bmatrix} \lambda_1 & 0 & 0 \\ 0 & \lambda_2 & 0 \\ 0 & 0 & \lambda_3 \end{bmatrix} \qquad \mathbf{E} = \begin{bmatrix} \varepsilon_{1x} & \varepsilon_{2x} & \varepsilon_{3x} \\ \varepsilon_{1y} & \varepsilon_{2y} & \varepsilon_{3y} \\ \varepsilon_{1z} & \varepsilon_{2z} & \varepsilon_{3z} \end{bmatrix}$$

The eigenvalues and eigenvectors represent the principal diffusion directions and diffusivity, respectively. The eigenvalues are real and non-negative due to the positive semi-definite nature of $\mathbf{D}$, and the corresponding eigenvectors form an orthonormal

basis [33]. The principal eigenvector associated with λ_1 points in the direction of greatest diffusivity (since $\lambda_1 \geq \lambda_2 \geq \lambda_3$). In perfect isotropic diffusion, all eigenvalues will be equal.

DTI Derived Metrics

After computing $\mathbf{D}$, several scalar metrics can be computed from the eigenvalues to summarize different aspects of water diffusion [34]. These metrics are rotationally invariant, meaning they do not change if the coordinate system is rotated.

Fractional anisotropy is a normalized measure of the degree of anisotropy. FA is 0 for isotropic diffusion and approaches 1 for fully anisotropic diffusion, according to:

$$FA = \sqrt{\frac{3}{2}} \cdot \frac{\sqrt{(\lambda_1 - \bar{\lambda})^2 + (\lambda_2 - \bar{\lambda})^2 + (\lambda_3 - \bar{\lambda})^2}}{\sqrt{\lambda_1^2 + \lambda_2^2 + \lambda_3^2}} \tag{2.2.7}$$

with $\bar{\lambda} = (\lambda_1 + \lambda_2 + \lambda_3)/3$.

Mean diffusivity represents the overall magnitude of diffusion and is calculated as the average of the three eigenvalues:

$$MD = \frac{1}{3}(\lambda_1 + \lambda_2 + \lambda_3) \tag{2.2.8}$$

Axial diffusivity corresponds to the principal eigenvalue, representing the diffusion along the primary axis of the tensor (which is assumed to align with the dominant fibre orientation):

$$AD = \lambda_1 \tag{2.2.9}$$

Radial diffusivity is the average of the two minor eigenvalues, representing

diffusion perpendicular to the principal axis:

$$RD = \frac{1}{2}(\lambda_2 + \lambda_3) \tag{2.2.10}$$

2.2.3 Diffusion Kurtosis Imaging

While DTI provides a rank-2 matrix to model diffusion, DKI models diffusion as a rank-4 tensor to characterize deviation from Gaussian diffusion. This tensor, $\mathbf{W}$, has the components:

$$\mathbf{W} = [W_{ijkl}], \quad i, j, k, l \in \{x, y, z\} \tag{2.2.11}$$

DKI was proposed by Jensen et al. in 2005, where the underlying theory was presented and parametric maps of excess diffusional kurtosis were first published [12]. It has since been used in a wide range of research and clinical applications, including neonatal brain development, multiple sclerosis, Parkinson's disease, and cancer grading [35–38]. In particular, DKI has shown promise in detecting early pathological changes that may not be apparent using conventional DTI metrics, such as in mild traumatic brain injury or preclinical stages of Alzheimer's disease [39, 40].

DKI requires longer acquisition times due to the need for multiple b-values and a high number of gradient directions, limiting its clinical practicality. DKI is also highly sensitive to noise, particularly at high b-values, which can lead to biased or physiologically implausible kurtosis estimates. Additionally, the model does not resolve multiple fibre populations and can yield inaccurate estimates in regions of complex fibre architecture.

Properties of the Diffusion Kurtosis Tensor

The kurtosis tensor is a rank-4 tensor with initially $3^4 = 81$ components. Due to the underlying symmetries in physical diffusion processes, the number of independent elements reduces to 15. These symmetries are:

1. Symmetry under index pair exchange within each pair:

$$W_{i,j,k,l} = W_{j,i,k,l} = W_{i,j,l,k}$$

2. Symmetry between index pairs:

$$W_{i,j,k,l} = W_{k,l,i,j}$$

These 15 elements, plus the 6 components of the diffusion tensor, result in a total of 21 parameters for DKI modelling. In general, at least 3 distinct b-values (including $b = 0$) and at least 15 distinct diffusion directions are required to solve the tensor.

In DKI, the Stejskal-Tanner equation is expanded to the second order [12]:

$$\ln(\frac{S(b, \mathbf{g})}{S_0}) = -bD(\mathbf{g}) + \frac{1}{6}b^2D^2(\mathbf{g})K(\mathbf{g}) \tag{2.2.12}$$

where,

- $S(b, \mathbf{g})$ is the signal at a given b-value and gradient direction $\mathbf{g}$
- S_0 is the signal at $b = 0$
- b is the b-value
- $D(\mathbf{g})$ is the apparent diffusion coefficient along $\mathbf{g}$
- $K(\mathbf{g})$ is the apparent kurtosis coefficient along $\mathbf{g}$

Solving for both parameters, $D(\mathbf{g})$ and $K(\mathbf{g})$, requires multi-shell data with at least two non-zero b-values. At low b-values (e.g., $b < 1000$ s/mm^2), the signal decay is dominated by the linear diffusion term $-bD$. At high b-values, the quadratic $\frac{1}{6}b^2D^2K$ term dominates and allows for kurtosis to be captured (Figure 2.4). Sampling across a range of b-values overdetermines the system, enabling stable and accurate fitting of the DKI model.

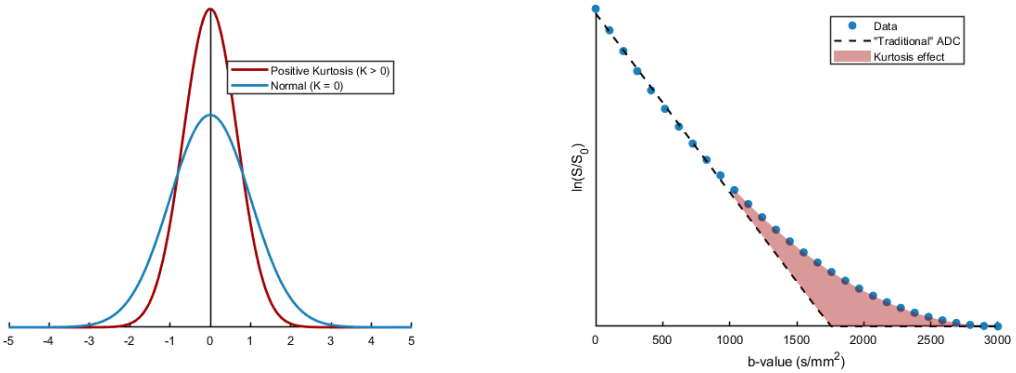

Figure 2.4: Illustrations of kurtosis, showing difference in "peakedness" (left). Diffusion kurtosis causes signal decay to deviate from the monoexponential model fit, seen in b-values > 1000 (right).

The kurtosis coefficient can be sampled from the fitted diffusion and kurtosis tensors by performing tensor contraction with the unit vector, $\mathbf{g}$:

$$K(\mathbf{g}) = \frac{MD^2}{D(\mathbf{g})^2} \sum_{i,j,k,l=1}^{3} g_i g_j g_k g_l W_{ijkl} \tag{2.2.13}$$

with

$$D(\mathbf{g}) = \sum_{i,j=1}^{3} g_i g_j D_{ij} \tag{2.2.14}$$

Physical Interpretation of Diffusion Kurtosis

Kurtosis is a statistical measure of the "tailedness" or "peakedness" of a probability distribution (Figure 2.4). $K(\mathbf{g})$ quantifies how the distribution of water displacements deviates from a normal distribution along a direction $\mathbf{g}$. Although inspired by statistical kurtosis, the diffusion kurtosis coefficient reflects physical properties of the displacement distribution rather than strictly statistical moments. A kurtosis value of zero corresponds to purely Gaussian diffusion, while positive kurtosis indicates a higher probability of small displacements and a sharper peak in the displacement distribution. In biological tissue, excess kurtosis is often attributed to barriers such as membranes, myelin sheaths, and cellular packing. Within a fibre-based phantom, kurtosis arises from restricted water diffusion within the interstitial spaces between tightly packed synthetic fibres. Regions of crossing fibres can increase kurtosis; Ankele & Schultz found that fibre crossings with varying angles (0° to 90°) caused increases in radial kurtosis up to a factor of 4.23 and axial kurtosis up to a factor of 5.65 compared to a single fibre configuration [41]. Negative kurtosis estimates are non-physical in most biological contexts and typically arise from noise, poor model fitting, or insufficient data sampling. This leads to many models restricting values to be positive.

DKI Derived Metrics

After computing $\mathbf{D}$ and $\mathbf{W}$, several rotationally invariant scalar metrics can be computed to characterize kurtosis within the diffusion.

Kurtosis fractional anisotropy is analogous to FA in DTI, such that KFA is 0

for isotropic kurtosis and approaches 1 for anisotropic kurtosis. It is defined as [42]:

$$KFA = \frac{||\mathbf{W} - \bar{W}\mathbf{I}^{(4)}||_F}{||\mathbf{W}||_F} \tag{2.2.15}$$

where $\bar{W}$ is the kurtosis tensor mean and $\mathbf{I}^{(4)}$ is the fully symmetric, rank-4 isotropic tensor.

Mean kurtosis is analogous to MD, with MK being defined as the average of directional kurtosis coefficient across all spatial directions. This can most easily be defined as a surface integral; however, in practice it is numerically resolved by averaging directional kurtosis values over a finite number of directions [43]:

$$MK = \frac{1}{4\pi}\int_{S^2} K(\mathbf{g})d\mathbf{g} \tag{2.2.16}$$

Axial kurtosis is analogous to AD and describes the kurtosis parallel to the principal diffusion direction [43]:

$$AK = K(\mathbf{e}_1) \tag{2.2.17}$$

Radial kurtosis is analogous to RD and describes the kurtosis orthogonal to the principal diffusion direction [43]:

$$RK = \frac{1}{2}[K(\mathbf{e}_2) + K(\mathbf{e}_3)] \tag{2.2.18}$$

2.2.4 Constrained Spherical Deconvolution

CSD is an advanced diffusion MRI technique designed to resolve multiple fibre populations within a single voxel. CSD estimates the fibre orientation distribution function, or fODF, a continuous function that describes the probability of diffusion occurring along different orientations on the unit sphere. Spherical deconvolution for diffusion imaging was first proposed by Tournier et al, where they assert that the average displacement of water molecules is expected to be on the order of 10 μm over the course of a diffusion-weighted scan [44]. This relatively small displacement implies that water molecules remain confined to a single fibre bundle, preventing signal mixing across distinct orientations. As such, the overall diffusion-weighted signal can be approximated as a sum of the signal from each of the different bundles. CSD also assumes that all fibre populations share identical diffusion characteristics, allowing them to be modelled using a single response function. The signal from a single coherently oriented fibre population can be measured and represented by an axially symmetric response function, $R(\theta)$, where θ is the elevation angle in spherical coordinates. The measured signal, $S(\theta, \phi)$ is the signal potentially containing several distinct fibre populations, where ϕ is the azimuthal angle in spherical coordinates. $S(\theta, \phi)$ can be modelled as the spherical convolution of the response function with the fODF, $F(\theta, \phi)$ [44]:

$$S(\theta, \phi) = F(\theta, \phi) \ \otimes \ R(\theta) \tag{2.2.19}$$

The fODF describes the relative volume fraction of fibres aligned along each direction (θ, ϕ) on the unit sphere (Figure 2.5). In the case of N distinct fibre populations, the fODF can be represented as the sum of N Dirac delta functions, each centred on a fibre orientation and scaled by its corresponding volume fraction.

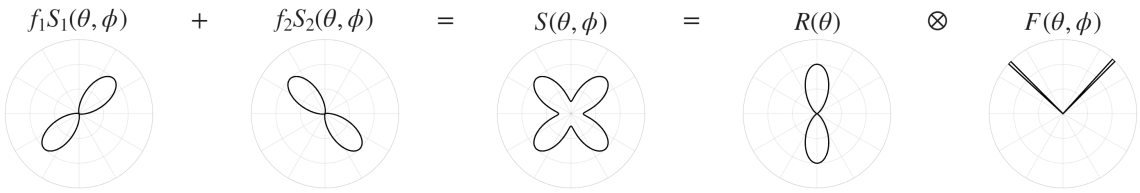

Figure 2.5: Conceptual overview of CSD, where the measured signal $S(\theta, \phi)$ is the linear combination of individual fibre contributions $f_1S_1(\theta, \phi) + f_2S_2(\theta, \phi)$ and modelled as a spherical convolution of a response function $R(\theta)$ with the fibre orientation distribution function $F(\theta, \phi)$.

CSD has become particularly valuable in tractography applications, where accurate mapping of white matter pathways is essential for studying connectivity in healthy and diseased brains [45–47]. Clinically, CSD has shown utility in pre-surgical planning, especially near there eloquent cortex where tracts may cross or converge. Its capacity to provide high-resolution orientation information makes it well-suited for exploring longitudinal changes in white matter architecture and for developing personalized connectivity-based biomarkers.

Despite its strengths, CSD relies on several simplifying assumptions that limit its accuracy in certain contexts. The method presumes that all fibre populations within a voxel share the same response function, typically derived from a single-fibre region, which may not hold in tissues with varying axon diameters, packing densities, or pathologies. Additionally, CSD does not model diffusivity explicitly, meaning it cannot distinguish between fibre populations with similar orientation but different diffusion characteristics. The fODF itself is a relative measure and lacks a direct biophysical interpretation, making quantitative comparisons across subjects or time points challenging without careful normalization. Moreover, CSD requires high angular resolution and sufficient SNR, and performance can degrade in voxels with low anisotropy or significant noise contamination, especially when overly aggressive

regularization is applied.

Spherical Harmonics Formulation

To efficiently solve the convolution problem in CSD, both the response function and the fODF are represented using a spherical harmonic (SH) basis. Spherical harmonics are the angular analog of the Fourier series on the sphere and provide a compact, orthonormal basis for representing functions defined over the unit sphere. In this framework, the fODF is expressed as a linear combination of SH functions [48]:

$$F(\theta, \phi) = \sum_{l=0}^{l_{max}} \sum_{m=-l}^{l} f_{lm} Y_l^m(\theta, \phi) \tag{2.2.20}$$

where $Y_l^m(\theta, \phi)$ are the SH functions of degree l and order m, and f_{lm} are the corresponding coefficients. As diffusion has antipodal symmetry, one fundamental property of the fODF is $F(\theta, \phi) = F(\pi - \theta, \phi + \pi)$. Only even ordered spherical harmonics ($l = 0, 2, 4, ...$) are symmetric about the origin, making them suited to represent diffusion. As such, l is restricted to even orders, updating the linear combination to:

$$F(\theta, \phi) = \sum_{l=0,2,4,...}^{l_{max}} \sum_{m=-l}^{l} f_{lm} Y_l^m(\theta, \phi) \tag{2.2.21}$$

Similarly, the measured signal can be represented as:

$$S(\theta, \phi) = \sum_{l=0,2,4,...}^{l_{max}} \sum_{m=-l}^{l} s_{lm} Y_l^m(\theta, \phi) \tag{2.2.22}$$

In addition to antipodal symmetry, the response function represented the diffusion profile of a single, coherently oriented fibre bundle, so it is assumed to have rotational symmetry, making it independent of the azimuthal angle ϕ. Functions that depend

only on θ are represented by the zonal harmonics, where $m = 0$. All other non-zero values of m will have coefficients of zero. The response function can be simplified to:

$$R(\theta) = \sum_{l=0,2,4,\ldots}^{l_{max}} r_l Y_l^0(\theta) \tag{2.2.23}$$

For each harmonic order l, the coefficients of $S(\theta, \phi)$ and $F(\theta, \phi)$ are written as vectors $\mathbf{s}_l$ and $\mathbf{f}_l$ of length $2l + 1$. The response function is written as a matrix $\mathbf{R}_l$ of size $(2l + 1) \times (2l + 1)$. The reason for SH representation can now be seen, since the spherical convolution can be reduced to a simple matrix multiplication:

$$\mathbf{s}_l = \mathbf{R}_l \cdot \mathbf{f}_l \tag{2.2.24}$$

Solving for $\mathbf{f}_l$ becomes a straightforward inverse problem, often solved with a simple linear least squares fit.

The number of SH coefficients, N, required to represent a function up to order l_{max} is:

$$N = \sum_{l=0,2,4,\ldots}^{l_{max}} (2l + 1) \tag{2.2.25}$$

In order to obtain a stable least-square fit, the number of gradient directions must meet or exceed this number. The number of directions for various l_{max} values is summarized below:

$l_{\max}$	N_{coeffs}
2	5
4	15
6	28
8	45
10	66
12	91

To allow for a sufficient number of SH coefficients, high angular resolution diffusion imaging (HARDI) data acquisition becomes critical. Unlike conventional DTI, which typically uses 6–30 gradient directions, HARDI acquires diffusion-weighted data along a much larger number of directions, often 45 or more. This dense angular sampling is necessary to estimate the fODF with sufficient precision, particularly when modelling complex fibre configurations. While HARDI is essential for CSD, it also benefits DTI by improving tensor estimation accuracy, reducing fitting error, and increasing robustness in regions with noise or subtle anisotropy. Even though DTI assumes Gaussian diffusion and a single principal direction, using more directions enhances the stability and reliability of derived scalar metrics such as FA and MD.

Constraints of CSD

In practice, the basic spherical deconvolution approach can produce physically implausible results, including negative values in the fODF. The constrained version of spherical deconvolution, introduced by Tournier et al. a few years after their initial

paper [13], enforces non-negativity constraints on the fODF:

$$F(\theta, \phi) \geq 0 \quad \forall\ \theta, \phi \tag{2.2.26}$$

To estimate the SH coefficients in CSD, the optimization problem is formulated as a regularized least-squares problem with a non-negativity constraint. An iterative approach is used to continue making improved estimates of the fibre orientation distribution function, using a modified Tikhonov regularisation method [49]:

$$\mathbf{f}_{i+1} = \arg\min\{\|\mathbf{X}\mathbf{f}_i - \mathbf{S}\|^2 + \lambda^2\|\mathbf{L}\mathbf{f}_i\|^2\} \tag{2.2.27}$$

where,

- $\mathbf{X}$ is the problem matrix, which maps SH coefficients to signal space and performs spherical convolution
- $\mathbf{f}_i$ represents the current SH coefficients of the fODF (the parameter to be estimated)
- $\mathbf{S}$ is the measured diffusion signal
- λ is a small Tikhonov regularization parameter to improve numerical stability
- $\mathbf{L}$ is a constraint matrix, which is updated iteratively and provides the current negative amplitudes of the fODF

The method operates iteratively: starting with an initial fODF estimate, negative amplitudes are identified across directional samples, and this constraint information is incorporated into the Tikhonov regularization framework to generate an improved estimate. Each iteration produces a refined fODF and updated constraint set until convergence is achieved, typically defined as no further or very minimal change in the

set of negative directions. This approach does not completely forbid negative fODF values, but does heavily penalize them. This yields a solution that preserves the data fidelity of the original spherical deconvolution while ensuring biological plausibility.

CSD-Derived Metrics

Several scalar and vector measures can be derived from the fODF estimated by CSD. One common metric is the generalized fractional anisotropy (GFA), defined as [50]:

$$\text{GFA} = \frac{\sqrt{N \sum_{i=1}^{N} (F_i - \bar{F})^2}}{\sqrt{(N-1) \sum_{i=1}^{N} F_i^2}} \tag{2.2.28}$$

where F_i is the fODF amplitude in direction i, $\bar{F}$ is the mean amplitude, and N is the number of sampled directions on the sphere. GFA quantifies the anisotropy of the fODF and ranges from 0 (isotropic diffusion) to 1 (strong directional preference).

2.2.5 Summary of Modelling Techniques

In summary, dMRI provides a powerful non-invasive tool for probing tissue microstructure through water displacement patterns. Foundational techniques like DWI and DTI have established clinical relevance and enable the quantification of scalar diffusion metrics under the assumption of Gaussian diffusion. Extensions such as DKI and CSD overcome these assumptions by modelling non-Gaussian behaviour and resolving multiple fibre populations, respectively. However, these higher-order models demand more intensive acquisition schemes (e.g., HARDI), are more sensitive to noise, and require careful parameter estimation.

Table 2.1: Summary of diffusion MRI models with key assumptions, acquisition needs, metrics, and main strengths and limitations.

Model	**Assumptions**	**Requirements**	**Key Metrics**	**Strengths and Limitations**
DWI	Monoexponential decay	3 directions, single shell	ADC	Simple; lacks directional info
DTI	Gaussian diffusion	$\geq$6 directions, single shell	FA, MD, AD, RD	Captures anisotropy; fails in crossing fibres
DKI	Non-Gaussian diffusion	$\geq$15 directions, multi-shell	MK, AK, RK, KFA	Models non-Gaussianity; noise-prone
CSD	Multiple fibre populations	$\geq$45 directions, single shell	GFA	Resolves crossings; assumes uniform response

Chapter 3

Review of dMRI Phantoms

Phantoms are essential tools in MRI for the validation, calibration, and standardization of acquisition protocols. Diffusion phantoms can be broadly categorized into two classes: isotropic and anisotropic phantoms. Isotropic phantoms are designed to emulate a simple diffusion environment without preferential diffusion orientation, allowing them to benchmark the accuracy of scalar diffusion metrics (like ADC). Anisotropic phantoms simulate more complex environments with directional dependence of diffusion, allowing them to validate diffusion tensor metrics (like FA or MD).

Several types of isotropic phantoms have been developed over the years; typically, these phantoms consist of containers filled with liquid or gels whose diffusivity properties are similar to biological tissues. Common materials include water-based solutions (e.g. polyvinylpyrrolidone (PVP), sucrose, polyethylene glycol), and gels (e.g. polyacrylamide, agarose) [51]. These phantoms can include smaller vials containing different concentrations of solution to demonstrate a range of ADC values.

The following section focuses specifically on anisotropic diffusion phantoms, with

an emphasis on their construction methods and quantitative evaluation of repeatability. This section aims to compile results from several studies to provide a basis of comparison for the results of this work. To find relevant papers, Web of Science was searched with the keywords "MRI phantom AND *metric* AND *model*", where *metric* was replaced with metrics of interest (e.g. CoV, ICC) and *model* was replaced with different models (e.g. DTI, DKI). Abstracts were reviewed to determine relevance, and studies were selected to reflect a range of phantom constructions and analysis methods that align with the goals of this review.

3.1 Phantom Designs

3.1.1 Capillary Arrays

Capillary array phantoms aim to mimic the restricted diffusion of axonal bundles by creating arrays of parallel hollow channels, which offer a controlled method for generating diffusion anisotropy. One of the earliest examples was presented by Yanasak & Allison, who used borosilicate glass capillaries with inner diameters of 23, 48, and 82µm arranged in a tight hexagonal packing [52]. They reported feasibility for DTI applications, although noted issues with signal dropout from trapped air and epoxy residue used in the manufacturing process. Kim et al. later developed a cylindrical capillary array phantom made of lead silicate glass with 50μm diameter pores and filled with distilled water [53]. While the phantom allowed repeatable FA and ADC measurements, they reported that the DTI metrics were sensitive to imaging parameters such as TE, b-value, and gradient directions, and that the FA and ADC values did not fully match those of brain tissue. Komlosh et al. used a GCA phantom

made from stacked, fused silica wafers with capillary pores ranging from 5–25µm [54]. The capillary arrays were placed in a polytetrafluoroethylene base and filled with decamethylcyclopentasiloxane, a viscous fluid selected for its low diffusivity. However, they found that for the largest (25µm) pores, diffusion appeared nearly free, and many spins did not interact with the pore walls during the diffusion time. As a result, attempts to simultaneously fit both diffusivity and pore diameter led to inaccurate estimates, highlighting a limitation in sensitivity when characterizing larger pore sizes. More recently, Witherspoon et al. leveraged high-resolution 3D printing to fabricate methyl methacrylate-based photoresin phantoms with 10µm pores [55]. These phantoms exhibited minimal susceptibility artifacts and were stable in water, but the fabrication process was time-consuming and required long development steps to clear uncrosslinked resin, representing a current practical limitation for large-scale phantom production.

3.1.2 Synthetic Fibres

Synthetic fibre phantoms represent another major category of diffusion MRI validation tools, utilizing various manufactured filaments to create controlled anisotropic environments that mimic white matter tracts. Unlike capillary arrays that rely on hollow channels, these phantoms employ solid fibres to generate diffusion anisotropy through the interstitial spaces between packed fibres. Commonly used materials include ultra-high-molecular-weight polyethylene (UHMWPE, e.g., Dyneema), polyamide (e.g., nylon/polyfil), polypropylene, and polyester.

Lorenz et al. conducted a comprehensive evaluation of five different fibre materials for their suitability as DTI phantoms, including hemp, linen, viscose rayon,

polyamide, and Dyneema [56]. Fibre diameters ranged from 22μm to 865 μm, depending on material. Each phantom was constructed by winding fibres into parallel bundles (170mm length, 20mm diameter) and enwrapping them with plastic ribbon underwater to prevent air bubble artifacts. Their findings demonstrated significant differences in diffusion properties between hydrophilic fibres (hemp, linen, viscose rayon) and hydrophobic fibres (polyamide, Dyneema). The hydrophobic fibres exhibited more consistent fractional anisotropy values and better directional alignment of the principal eigenvector with the actual fibre orientation. The authors attributed these differences to the hydrophilic fibres' tendency to absorb water, causing expansion and variation in local fibre direction, whereas hydrophobic fibres maintained their structure and provided greater restriction to water diffusion.

One of the key advantages of synthetic fibre phantoms is the flexibility in constructing a wide range of geometries, enabling the design of complex configurations such as varying fibre densities, orientations, and crossing angles. Pullens et al. constructed a polyester-based phantom using bundles of yarn shrink-wrapped in tubing, achieving crossing angles of 30°, 50°, and 65° [57]. Farrher et al. designed a multi-section Dyneema phantom with three distinct compartments: (1) parallel fibres with uniform density, (2) parallel fibres with a density gradient, and (3) crossing fibres at a 90° angle [58]. The 8µm fibres were wound around a Plexiglass support structure and immersed in water. Simard et al. studied the PreOperative Performance phantom, which in that version, contained bifurcating and 90° fibre modules as its main features [14].

Notably, Tachibana et al. compared a simple Dyneema phantom against a glass capillary plate, concluding that Dyneema is more appropriate as a standard DTI QC

phantom since the FA and MD values obtained were more comparable to those of white matter in the brain [59].

Despite their advantages, synthetic fibre phantoms have several limitations. Most designs only simulate diffusion in the spaces between fibres and do not capture key biological features such as intra-axonal diffusion, membrane permeability, or compartmental exchange [57]. Additionally, construction can be technically demanding, and factors like uneven fibre packing, alignment errors, or material degradation over time can introduce variability.

3.2 Phantom Validation

To evaluate the repeatability of the PreOperative Performance phantom in a greater context, a review of prior diffusion phantom studies was conducted. Table 3.1 summarizes the phantom construction, models, and reported validation metrics used in these studies when available.

Overall, the literature demonstrates that anisotropic diffusion phantoms can provide strong measurement reproducibility for conventional DTI metrics, particularly FA and MD, with CoV values frequently reported below 5%. However, the extent of reproducibility depends heavily on phantom design. Phantoms with uniform fibre orientations and consistent packing, such as polyamide or UHMWPE, tend to yield the lowest variability. In contrast, designs with heterogeneous features like variable fibre density or crossing angles often report higher CoV values, sometimes exceeding 10–15%.

Several studies have also extended validation to higher-order models such as DKI, showing that kurtosis metrics are more sensitive to noise and acquisition differences.

Table 3.1: Anisotropic diffusion phantom repeatability metrics found in the literature

Reference	**Phantom**	**Model(s)**	**Metric(s)**	**Metric Values**
Teipel et al. (2011) [60]	Polyamide (polyfil) fibres arranged in a ring	DTI	FA	FA CoV: 5.2–9.8%
Hakulinen et al. (2012) [61]	Polyamide (polyfil) fibres arranged in a ring	DTI	FA	FA CoV: 1.3–2.1%
Wilde et al. (2018) [62]	Polymer textile hollow fibres with variable fibre density and tract size	DTI	FA	FA CoV: 4.48–14.88%
Provenzale et al. (2018) [63]	Polypropylene yarn with variable fibre density and tract size	DTI	FA	FA CoV: 2.42–5.59%
de Souza et al. (2019) [64]	Dyneema fishing line with variable filament diameters	DTI	FA, MD	FA CoV: 0.47–4.3% MD CoV: 0.97–3.68%
Kimura et al. (2020) [65]	UHMWPE with variable fibre density bundles	DTI	FA	FA CoV: 1.00–1.89%
Kasa et al. (2020) [66]	3D-printed porous polymer with variable crossing angles (30°–90°)	DTI DKI	MD, AD, RD, MK, AK, RK	MD CoV: ∼1–6% AD CoV: ∼0.75–2.5% RD CoV: ∼1–8.75% MK CoV: ∼0.75–4% AK CoV: ∼1.25–6% RK CoV: ∼0.75–7.75%
Mushtaha et al. (2021) [67]	3D-printed axon-mimetic phantom using GEL-LAY porous filament	DTI DKI	FA, MD, AD, RD, AK, RK, MK	FA CoV: 6.58% MD CoV: 4.88% AD CoV: 2.41% RD CoV: 7.57% MK CoV: 3.62% AK CoV: 15.00% RK CoV: 5.78%

Among DKI-derived measures, MK, AK, and RK exhibit substantially higher CoVs than FA or MD, often ranging from 5–15%, with some values surpassing 20% in regions with crossing fibres or branching geometries. These trends reflect the additional instability introduced by estimating fourth-order tensor components. To date, however, no studies have assessed the reproducibility of orientation-resolved diffusion models, such as CSD, using physical phantoms.

Taken together, this review highlights that while many phantom designs can support robust DTI reproducibility, reliable validation of advanced diffusion models remains more challenging. To build on the literature, this thesis evaluates the PreOperative Performance phantom for a wide range of scalar metrics, with a particular focus on the repeatability of both standard and advanced dMRI models.

Chapter 4

Materials and Methods

4.1 Phantom Description

The PreOperative Performance Phantom 5 (version POP-0005-001, Toronto, ON) was used throughout the study (Figure 4.1). The phantom consists of a sealed polymethyl methacrylate housing (height = 172mm, outer diameter = 178mm) filled with polyvinyl alcohol (PVA) solution doped with gadolinium and a preservative. Inside, arrays of fixed synthetic filaments are organized into different modules, including linear, bifurcating, and crossing fibre bundle geometries. The individual filaments have a diameter of 2μm and the fibre bundles have diameters ranging from 2.4–6.9mm. Isotropic modules filled with PVP at varying concentrations are used to represent different ADC values.

Figure 4.1: Front, lateral, and rear view photographs of the PreOperative Performance phantom.

4.2 Data Acquisition

Data was collected on a 3.0 T GE Discovery MR 750 (system software version 29.1, GE HealthCare, Milwaukee, WI) using a 32-channel head coil located in the Imaging Research Centre at St. Joseph's Healthcare Hamilton. The phantom was imaged across 11 independent trials, with complete removal and repositioning between each scan. A level was used to achieve approximately the same phantom positioning between trials, however, the positioning was not strictly controlled to emulate realistic QA scenarios.

All scans were conducted with consistent acquisition parameters and there were no major changes to scanner hardware or software across trials. The total scan time per trial was 69 minutes 38 seconds. The entire scanning protocol consists of:

1. **Localizer scan** (0 min 21 sec): Localizer images were acquired using a 3-plane fast gradient echo (FGE) sequence (TR/TE = 5.5/1.7ms, flip angle = 30°, FOV = 26cm, matrix = 256×256, slice thickness = 5.0mm, number of slices = 25).

2. **T1-weighted anatomical scan** (4 min 37 sec): High-resolution axial 3D images were acquired using a fast spoiled gradient echo (FSPGR) sequence

(TR/TE = 7.94/3.07 ms, flip angle = 12°, FOV = 24cm, matrix = 240×240, voxel size = 1mm isotropic, number of slices = 168).

3. **3 direction PROPELLER DWI scan** (4 min 57 sec): Diffusion weighted imaging was acquired using a PROPELLER sequence (3 gradient directions, b-value = 1000 s/mm^2, number of b-zero volumes = 1, TR/TE = 11000/58.15 ms, flip angle = 110°, FOV = 24cm, matrix = 96×96, voxel size = 2.5mm isotropic, number of slices = 66)

4. **30 direction DTI scan** (4 min 5 sec): Diffusion tensor imaging was acquired using a spin-echo echo-planar sequence (30 gradient directions, b-value = 1000 s/mm^2, number of b-zero volumes = 3, TR/TE = 7000/58.1 ms, flip angle = 90°, FOV = 24cm, matrix = 96×96, voxel size = 2.5mm isotropic, number of slices = 66)

5. **60 direction HARDI scan** (7 min 35 sec): High angular resolution diffusion imaging was acquired using a spin-echo echo-planar sequence (60 gradient directions, b-value = 1300 s/mm^2, number of b-zero volumes = 3, TR/TE = 7000/61.6 ms, flip angle = 90°, FOV = 24cm, matrix = 96×96, voxel size = 2.5mm isotropic, number of slices = 66)

6. **90 direction HARDI scan** (11 min 5 sec): High angular resolution diffusion imaging was acquired using a spin-echo echo-planar sequence (90 gradient directions, b-value = 1300 s/mm^2, number of b-zero volumes = 3, TR/TE = 7000/61.6 ms, flip angle = 90°, FOV = 24cm, matrix = 96×96, voxel size = 2.5mm isotropic, number of slices = 66)

7. **30 direction DKI scan** (32 min 40 sec): Multi-shell diffusion kurtosis imaging

was acquired using a spin-echo echo-planar sequence (30 gradient directions, b-values = 250, 500, 750, 1000, 1500, 2000, 2500, 3000 s/mm^2, number of b-zero volumes = 3, TR/TE = 8000/75.1 ms, flip angle = 90°, FOV = 24cm, matrix = 96×96, voxel size = 2.5mm isotropic, number of slices = 66)

8. **B_0 map** (2 min 12 sec): Static magnetic field inhomogeneities were measured using a 2D gradient echo (GRE) sequence (TR/TE = 100/4.61ms, flip angle = 20°, FOV = 24cm, matrix = 128×128, slice thickness = 3.0mm, slice gap = 1.5mm, number of slices = 38)

9. **B_1^+ map** (2 min 4 sec): B_1^+ mapping was acquired using a 2D GRE sequence (TR/TE = 18/7.9ms, flip angle = 20°, FOV = 24cm, matrix = 128×128, slice thickness = 5.0mm, slice gap = 1.5mm, number of slices = 26)

4.3 Data Analysis

For the bulk of data analysis, DIPY (version 1.9.0) was used. DIPY is an open-source Python library for dMRI analysis, including reconstruction methods such as DTI, DKI, and CSD, as well as the ability to compute various diffusion-related metrics. It was selected for its integration with Windows systems and its well-documented, modular structure.

In addition, the FMRIB Software Library (FSL) was used for specific preprocessing tasks. FSL is an open-source software suite designed for preprocessing, analyzing, and visualizing MRI data. It was chosen in particular for its eddy current correction and image registration capabilities.

4.3.1 Preprocessing

The resulting images were downloaded in Digital Imaging and Communications in Medicine (DICOM) format and converted to Neuroimaging Informatics Technology Initiative (NIFTI) format using the `dcm2niix` tool. Preprocessing steps include denoising using DIPY's Marchenko–Pastur Principal Component Analysis (MP-PCA) algorithm, followed by eddy current correction with FSL's `eddy` tool. No additional preprocessing steps were applied (such as motion correction or susceptibility-induced distortions) since these are not relevant to a stationary phantom with low magnetic susceptibility differences.

A binary mask was generated to isolate the phantom from the background signal and restrict modelling to the area of interest, improving processing time. For each trial, a central slice from the 30-direction DTI scan was extracted and a background region of interest (ROI) was drawn. The maximum intensity value within the ROI was selected as a threshold. A 2D Gaussian blur (σ = 1.5, kernel size = 3×3) was applied to the data to reduce noise and improve spatial coherence. A preliminary mask was generated by including any pixel that was greater than the threshold.

Since the phantom object is cylindrical, the mask was cleaned using image processing techniques to match the expected shape. Morphological closing (kernel size = 9×9) was used to fill larger internal holes and flood filling was used to fill smaller holes. Only the largest connected component was retained, leaving a clean separation between the phantom object and the background (Figure 4.2). Each mask was visually inspected for accuracy. The phantom object was not moved between scans, so the same mask could be applied to all dMRI data in the same trial.

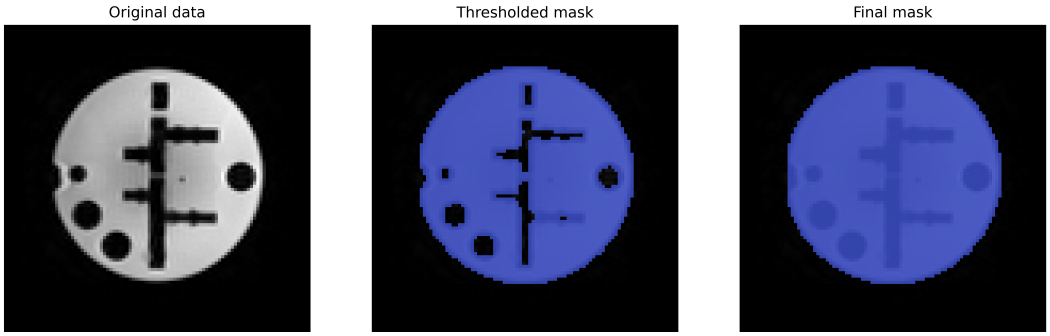

Figure 4.2: Binary mask generation through thresholding and image processing

4.3.2 Modelling

DTI and HARDI data were processed using DIPY's `TensorModel`, which models the diffusion signal assuming Gaussian displacement of water molecules within each voxel. The output is a rank-2 diffusion tensor, **D**.

DKI data was processed using DIPY's `DiffusionKurtosisModel`, which extends the diffusion tensor model to capture non-Gaussian diffusion effects. The output is a rank-4 tensor, **W**, that characterizes the excess kurtosis along various orientations.

To resolve multiple fibre orientations for the DTI and HARDI data, CSD was applied using DIPY's `ConstrainedSphericalDeconvModel`. An ROI (size = $10\times10\times10$, FA threshold = 0.7) was manually selected from a region containing a coherent, single-fibre structure in the phantom. (Figure 4.3). The model fitting was performed using regularized spherical harmonics with order $l_{max} = 8$. The output is the spherical harmonic coefficients at each voxel.

4.3.3 Postprocessing

After fitting each model, scalar diffusion metric maps were computed to perform quantitative comparisons across trials. For DTI, this included fractional anisotropy

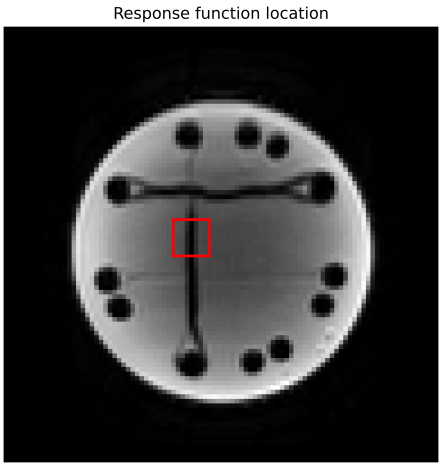

Figure 4.3: Location of response function

(FA), mean diffusivity (MD), axial diffusivity (AD), and radial diffusivity (RD). For DKI, derived metrics included kurtosis fractional anisotropy (KFA), mean kurtosis (MK), axial kurtosis (AK), and radial kurtosis (RK). For CSD, generalized fractional anisotropy (GFA) was calculated from the spherical harmonic coefficients. To enable voxel-wise comparison across repeated scans, all scalar metric maps were coregistered to a common space using FSL's `flirt` tool. An affine 12 parameter model was applied using the first trial as a reference volume. The same transformation was applied to all maps to maintain spatial consistency.

Six 3×3×3 voxel ROIs (yielding 27 values) were drawn on locations with a variety of fibre geometry (Figure 4.4):

- **ROI 1**: 45° intersection in the XZ plane. Bundle diameter is 4.0mm.
- **ROI 2**: 30° intersection in the XY plane. Bundle diameter is 4.5mm.
- **ROI 3**: Fibre splitting into 3 smaller fibre bundles. Two fibres split into the XY plane (seen in Figure 4.4) and one fibre splitting out-of-plane. Original fibre

diameter is 6.9mm and smaller fibre bundles are 2.9, 3.7, and 4.2mm.

- **ROI 4**: 90° intersection in the XY plane. Bundle diameter is 2.4mm.
- **ROI 5**: Simple linear fibre in the X plane. Bundle diameter is 4.3mm.
- **ROI 6**: Isotropic area with no fibres present

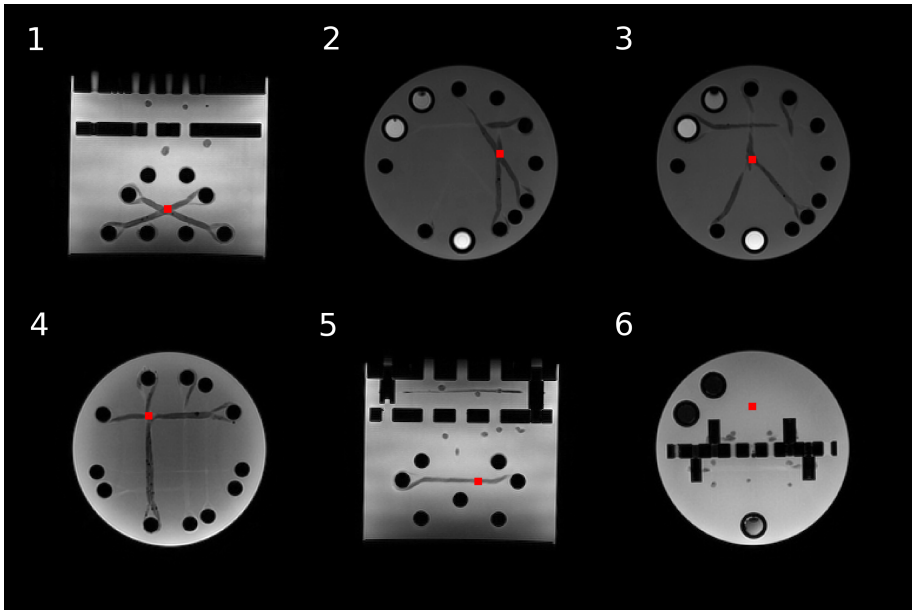

Figure 4.4: Locations of ROIs

4.4 Statistical Analysis

To assess the repeatability of diffusion metrics across repeated phantom scans, statistical analyses were conducted on the scalar maps derived from each diffusion model (DTI, DKI, and CSD). For each of the six ROIs, the mean (μ) and standard deviation (SD, σ) of each metric were computed across all 11 trials. From these values,

the coefficient of variation (CoV) was calculated to quantify the relative variability within each ROI:

$$CoV = \frac{\sigma}{\mu} \times 100\% \tag{4.4.1}$$

To summarize the overall repeatability for each diffusion metric and model, the average CoV across all ROIs was computed. The intraclass correlation coefficient (ICC) was also calculated, which estimates the proportion of total variance that is attributable to variance between ROIs (true variance) rather than within ROI variance across trials (error). A high ICC value (closer to 1) indicates that variation between scans is low relative to the variation between ROIs. Conversely, a low ICC indicates poor scan-to-scan repeatability. The general formula for ICC is:

$$ICC = \frac{\sigma^2_{between}}{\sigma^2_{between} + \sigma^2_{within}} \tag{4.4.2}$$

A two-way mixed-effects model was used, since the 11 scan trials were performed on a fixed system under controlled conditions and not randomly selected as part of a larger set of trials. This is denoted as ICC(3,1) and defined as:

$$ICC(3,1) = \frac{MS_{subjects} - MS_{error}}{MS_{subjects} + (k-1)MS_{error}} \tag{4.4.3}$$

where:

- $MS_{subjects}$ is the mean square for the subjects (ROIs)
- MS_{error} is the mean square error (residual variance)
- k is the number of measurements (11)

ICC values were interpreted according to standard guidelines:

- ICC < 0.50: poor reliability

- $0.5 \leq \text{ICC} < 0.75$: moderate reliability
- $0.75 \leq \text{ICC} < 0.90$: good reliability
- $\text{ICC} \leq 0.90$: excellent reliability

Chapter 5

Results

5.1 Rank-2 Diffusion Tensor Metrics

FA, MD, AD, and RD values were calculated for all 6 ROIs and across the three single-shell acquisition schemes (DTI, HARDI-60, and HARDI-90). The mean, standard deviation, and CoV for each individual ROI can be found below (Table 5.1–5.4). The average CoV for the six ROIs and ICC are also reported (Table 5.5). Boxplots showing the spread of data can be found in Appendix B.

Table 5.1: Comparison of FA values across ROIs and scanning protocols

	DTI			**HARDI-60**			**HARDI-90**		
	Mean	SD	CoV(%)	Mean	SD	CoV(%)	Mean	SD	CoV(%)
ROI 1	0.16	0.02	14.42	0.16	0.02	11.02	0.15	0.02	10.97
ROI 2	0.25	0.02	8.21	0.25	0.02	7.47	0.25	0.02	7.86
ROI 3	0.17	0.02	11.67	0.17	0.02	11.22	0.17	0.02	10.92
ROI 4	0.17	0.02	10.99	0.17	0.02	11.90	0.17	0.02	10.29
ROI 5	0.13	0.01	8.89	0.13	0.01	9.39	0.12	0.01	8.02
ROI 6	0.05	0.00	1.22	0.05	0.00	2.54	0.05	0.00	0.45

Table 5.2: Comparison of MD values across ROIs and scanning protocols

	DTI			**HARDI-60**			**HARDI-90**		
	Mean*	SD*	CoV(%)	Mean*	SD*	CoV(%)	Mean*	SD*	CoV(%)
ROI 1	1.44	0.05	3.56	1.44	0.05	3.16	1.46	0.05	3.26
ROI 2	1.37	0.03	2.04	1.37	0.03	1.91	1.38	0.03	1.93
ROI 3	1.49	0.04	2.74	1.49	0.04	2.65	1.51	0.04	2.78
ROI 4	1.43	0.04	2.81	1.42	0.04	2.74	1.44	0.04	2.59
ROI 5	1.56	0.02	1.27	1.56	0.02	1.23	1.56	0.02	1.15
ROI 6	1.75	0.01	0.43	1.76	0.01	0.43	1.77	0.01	0.49

*Mean and SD values are reported in units of $\times 10^{-3}$ mm^2/s

Table 5.3: Comparison of AD values across ROIs and scanning protocols

	DTI			**HARDI-60**			**HARDI-90**		
	Mean*	SD*	CoV(%)	Mean*	SD*	CoV(%)	Mean*	SD*	CoV(%)
ROI 1	1.66	0.04	2.80	1.65	0.04	2.26	1.66	0.04	2.16
ROI 2	1.67	0.03	1.55	1.66	0.03	1.65	1.67	0.02	1.44
ROI 3	1.72	0.03	1.75	1.71	0.03	1.54	1.73	0.03	1.71
ROI 4	1.61	0.04	2.46	1.61	0.04	2.28	1.62	0.04	2.57
ROI 5	1.73	0.02	1.00	1.73	0.02	0.93	1.74	0.04	2.57
ROI 6	1.81	0.01	0.41	1.83	0.01	0.46	1.85	0.01	0.48

*Mean and SD values are reported in units of $\times 10^{-3}$ mm^2/s

Table 5.4: Comparison of RD values across ROIs and scanning protocols

	DTI			**HARDI-60**			**HARDI-90**		
	Mean*	SD*	CoV(%)	Mean*	SD*	CoV(%)	Mean*	SD*	CoV(%)
ROI 1	1.36	0.06	4.09	1.34	0.05	3.88	1.34	0.06	4.27
ROI 2	1.24	0.03	2.55	1.22	0.03	2.42	1.23	0.03	2.65
ROI 3	1.40	0.05	3.58	1.38	0.05	3.47	1.38	0.05	3.50
ROI 4	1.34	0.04	2.99	1.33	0.05	3.43	1.34	0.05	3.34
ROI 5	1.47	0.02	1.53	1.47	0.03	1.73	1.47	0.02	1.67
ROI 6	1.73	0.01	0.50	1.72	0.01	0.43	1.72	0.01	0.44

*Mean and SD values are reported in units of $\times 10^{-3}$ mm^2/s

Table 5.5: Summary of repeatability metrics (CoV and ICC) for DTI-derived scalar measures across three single-shell acquisition protocols (DTI, HARDI-60, HARDI-90)

	DTI		**HARDI-60**		**HARDI-90**	
	CoV(%)	ICC	CoV(%)	ICC	CoV(%)	ICC
FA	9.23	0.9155	8.92	0.9335	8.08	0.9415
MD	2.14	0.9315	2.02	0.9417	2.03	0.9380
AD	1.66	0.8321	1.52	0.8846	1.60	0.8957
RD	2.54	0.9418	2.56	0.9469	2.64	0.9424

5.2 Rank-4 Diffusion Kurtosis Metrics

KFA, MK, AK, and RK values were calculated for all 6 ROIs using the multi-shell DKI acquisition. The individual ROI means, SD, and CoV can be found below (Table 5.6) as well as mean CoV and ICC (Table 5.7). Individual ROI boxplots can be found in Appendix B.

5.3 Constrained Spherical Deconvolution

GFA was calculated for all 6 ROIs and across the three single-shell acquisition schemes (DTI, HARDI-60, and HARDI-90) using CSD. ROI-specific GFA values (Table 5.8) and a summary of mean CoV and ICC (Table 5.9) is reported below. Boxplots for individual ROI data can be found in Appendix B.

Table 5.6: Comparison of kurtosis metrics across ROIs

	KFA			**MK**		
	Mean	SD	CoV(%)	Mean	SD	CoV(%)
ROI 1	0.45	0.04	8.27	0.27	0.04	15.05
ROI 2	0.47	0.05	9.69	0.24	0.03	14.39
ROI 3	0.43	0.02	4.54	0.21	0.02	10.06
ROI 4	0.44	0.04	8.83	0.23	0.04	15.78
ROI 5	0.59	0.07	11.11	0.15	0.04	27.02
ROI 6	0.17	0.00	1.73	0.07	0.01	7.63
	AK			**RK**		
	Mean	SD	CoV(%)	Mean	SD	CoV(%)
ROI 1	0.29	0.04	12.32	0.25	0.04	17.18
ROI 2	0.22	0.03	12.31	0.27	0.04	16.44
ROI 3	0.17	0.03	16.06	0.25	0.03	10.52
ROI 4	0.24	0.03	11.27	0.22	0.04	18.57
ROI 5	0.15	0.03	20.90	0.15	0.05	36.37
ROI 6	0.06	0.01	11.40	0.04	0.01	12.61

Table 5.7: Summary of repeatability metrics (CoV and ICC) for DKI-derived scalar measures (KFA, MK, AK, RK) across repeated trials.

	DKI	
	CoV(%)	ICC
KFA	7.36	0.9361
MK	14.99	0.8358
AK	14.04	0.9211
RK	18.62	0.8348

Table 5.8: Comparison of GFA values across ROIs and scanning protocols

	DTI			**HARDI-60**			**HARDI-90**		
	Mean	SD	CoV(%)	Mean	SD	CoV(%)	Mean	SD	CoV(%)
ROI 1	0.18	0.02	9.71	0.18	0.01	4.14	0.19	0.01	7.45
ROI 2	0.21	0.01	5.71	0.17	0.01	5.17	0.17	0.01	4.10
ROI 3	0.20	0.01	11.67	0.21	0.01	5.64	0.20	0.01	6.32
ROI 4	0.15	0.01	7.14	0.21	0.01	2.65	0.22	0.01	3.39
ROI 5	0.14	0.01	5.49	0.14	0.01	5.48	0.14	0.01	3.09
ROI 6	0.03	0.00	5.43	0.03	0.00	3.27	0.00	0.00	5.37

Table 5.9: Summary of repeatability metrics (CoV and ICC) for CSD-derived scalar measures across three single-shell acquisition protocols (DTI, HARDI-60, HARDI-90)

	DTI		**HARDI-60**		**HARDI-90**	
	CoV(%)	ICC	CoV(%)	ICC	CoV(%)	ICC
GFA	6.69	0.6603	4.39	0.8046	4.95	0.8507

5.3.1 fODF Peaks

To qualitatively assess the performance of CSD in resolving multiple fibre orientations, fODFs were visualized for each of the six regions of interest. In each ROI, a 5×5 field of surrounding voxels is shown alongside a highlighted voxel where fibre peak data was extracted. Fibre crossing angles were calculated from the direction vectors and compared to the known fibre geometry, where applicable.

The highlighted voxel in **ROI 1** exhibited two fibre peaks with the direction vectors:

$$\vec{f_1} = \begin{bmatrix} -0.672 \\ 0.717 \\ 0.188 \end{bmatrix} \quad \vec{f_2} = \begin{bmatrix} -0.999 \\ -0.039 \\ 0.012 \end{bmatrix}$$

The corresponding peak strengths were 5.459 and 3.440, respectively. The angle between the two vectors was calculated to be 49.8°, which corresponds to an error of 4.8° compared to the expected crossing angle of 45° (Figure 5.1).

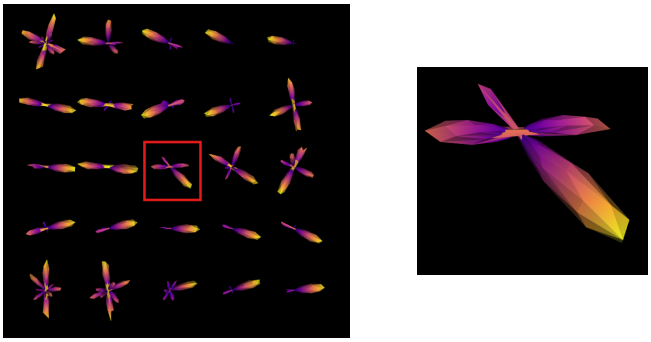

Figure 5.1: fODF peaks in ROI 1. Centre voxel shows 45° fibre intersection.

The voxel in **ROI 2** exhibited only one fibre peak with the direction vector:

$$\vec{f_1} = \begin{bmatrix} -0.499 \\ 0.858 \\ 0.121 \end{bmatrix}$$

The corresponding peak strength was 9.689. This demonstrates that the CSD model was not able to resolve a 30° intersection, and instead modelled the intersection as a collection of single-direction fibres (Figure 5.2).

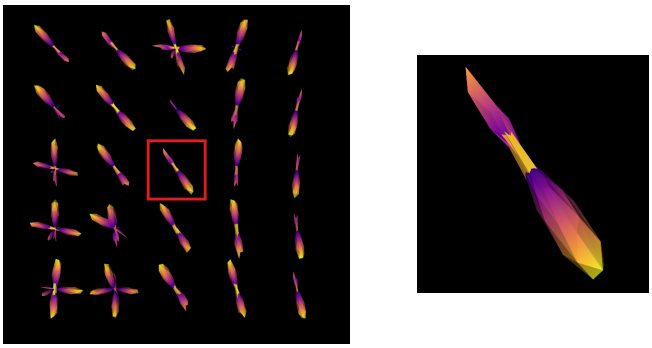

Figure 5.2: fODF peaks in ROI 2. Centre voxel shows one peak, failing to resolve the 30° intersection.

ROI 3 exhibited three fibre peaks with the direction vectors:

$$\vec{f_1} = \begin{bmatrix} 0.132 \\ 0.990 \\ 0.047 \end{bmatrix} \quad \vec{f_2} = \begin{bmatrix} 0.091 \\ -0.772 \\ 0.629 \end{bmatrix} \quad \vec{f_3} = \begin{bmatrix} 0.928 \\ -0.372 \\ 0.031 \end{bmatrix}$$

The corresponding peak strengths were 6.731 and 4.295, and 4.007 respectively. The angle between the vectors were 136.17° (fibre 1 & 2), 104.11° (2 & 3), 66.99° (1 & 3). This approximates the angles that would be expected for modelling a "Y" shaped bifurcation that included an third out-of-plane fibre (Figure 5.3).

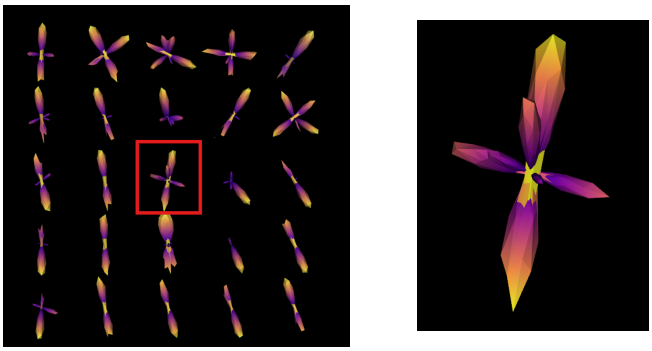

Figure 5.3: fODF peaks in ROI 3. Centre voxel shows three fibre peaks with out-of-plane elements.

ROI 4 exhibited two fibre peaks with the direction vectors:

$$\vec{f_1} = \begin{bmatrix} -0.999 \\ -0.039 \\ 0.012 \end{bmatrix} \quad \vec{f_2} = \begin{bmatrix} -0.121 \\ 0.900 \\ 0.295 \end{bmatrix}$$

The corresponding peak strengths were 6.490 and 5.968, respectively. The angle between the two vectors was 84.63°, which corresponds to an error of 5.37° compared to the ideal 90° (Figure 5.4).

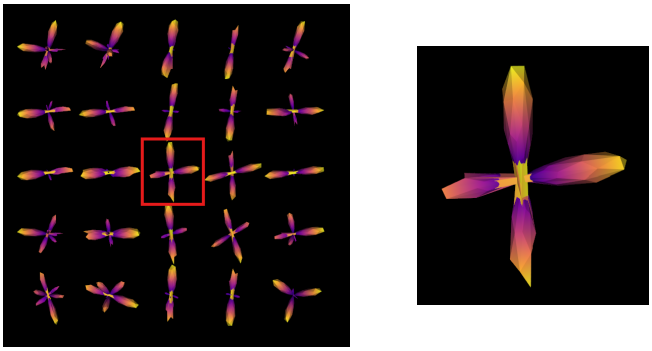

Figure 5.4: fODF peaks in ROI 4. Centre voxel shows two 90° fibre peaks.

ROI 5 had only one fibre peak with a strength of 12.444 and the direction vector:

$$\vec{f_1} = \begin{bmatrix} 0.987 \\ 0.124 \\ 0.102 \end{bmatrix}$$

This is expected since this ROI is from a simple linear fibre population (Figure 5.5).

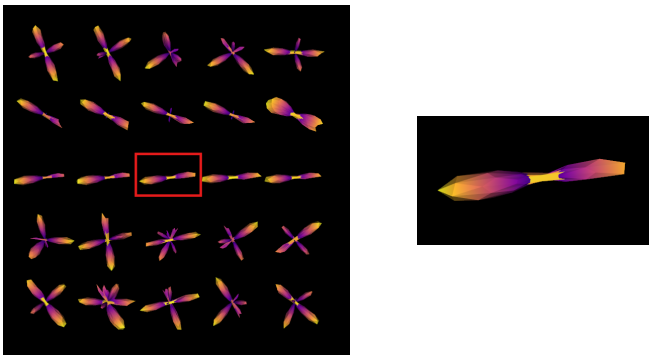

Figure 5.5: fODF peaks in ROI 5. Centre voxel shows one coherent fibre peak.

ROI 6 exhibited five fibre peaks with the direction vectors (Figure 5.6):

$$\vec{f_1} = \begin{bmatrix} 0.861 \\ 0.411 \\ 0.301 \end{bmatrix} \quad \vec{f_2} = \begin{bmatrix} -0.252 \\ -0.968 \\ 0.011 \end{bmatrix} \quad \vec{f_3} = \begin{bmatrix} -0.554 \\ 0.754 \\ 0.354 \end{bmatrix} \quad \vec{f_4} = \begin{bmatrix} -0.949 \\ 0.306 \\ 0.079 \end{bmatrix} \quad \vec{f_5} = \begin{bmatrix} -0.143 \\ -0.668 \\ 0.730 \end{bmatrix}$$

The corresponding peak strengths were 9.928, 6.638, 6.606, 6.329, and 4.995, respectively. The angle between the vectors ranged from 38.41° to 131.87°.

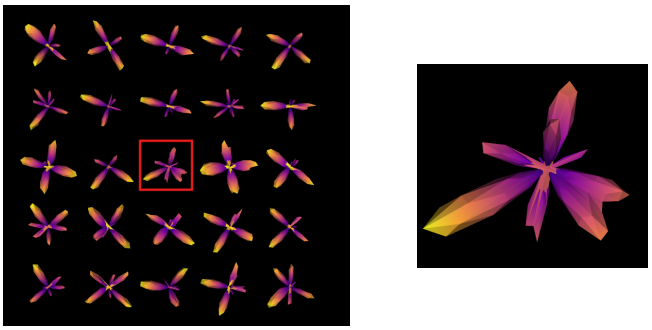

Figure 5.6: fODF peaks in ROI 6. Centre voxel shows five peaks, representing isotropic diffusion.

5.4 Scanner Stability

To assess scanner stability and ensure that temporal drift did not influence metric repeatability, maps of ΔB_0 and B_1^+ were evaluated. Consistency in B_0 and B_1^+ fields are essential, as field inhomogeneities can bias signal attenuation and thus compromise the accuracy of diffusion metrics. For the first 4 trials, these maps were regrettably not obtained, so the reported values are only across 7 trials. Figure 5.7 shows a representative ΔB_0 and B_1^+ maps from a single trial, confirming uniform spatial distribution. Some local non-uniformity can be seen at the fibre anchoring points. This is due to trapped internal air creating sharp susceptibility boundaries, but these artifacts would not be included in any of the assessed ROIs.

Across trials, ΔB_0 within the phantom exhibited a mean offset of -6.84 Hz with a standard deviation of 6.63 Hz, while B_1^+ had a mean of 211.35 μT and a standard deviation of 1.58 μT (Figure 5.8). These results indicate very little variation in both the static field (B_0) and transmit field (B_1^+), suggesting that the scanner environment remained stable over the repeated acquisitions.

While corrections for ΔB_0 and B_1^+ inhomogenities were not applied during diffusion model fitting or scalar metric calculations, the minimal variation observed

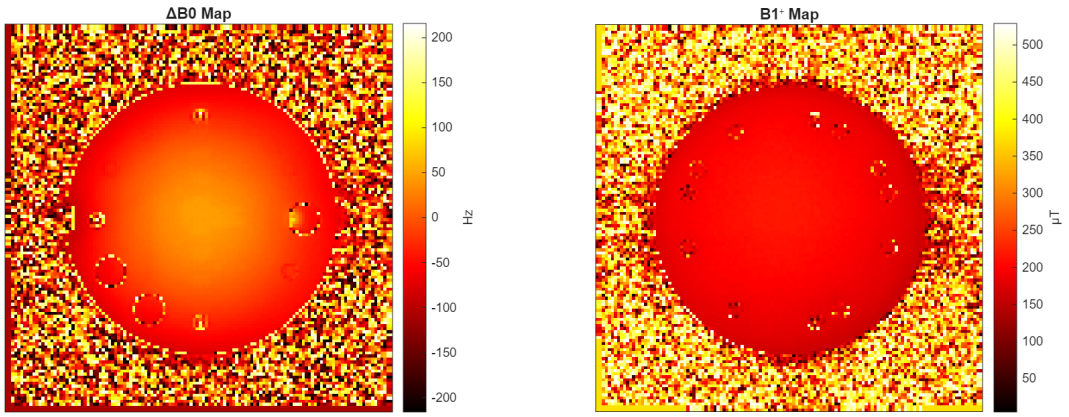

Figure 5.7: Representative ΔB_0 and B_1^+ maps showing uniformity of spatial distribution within the phantom

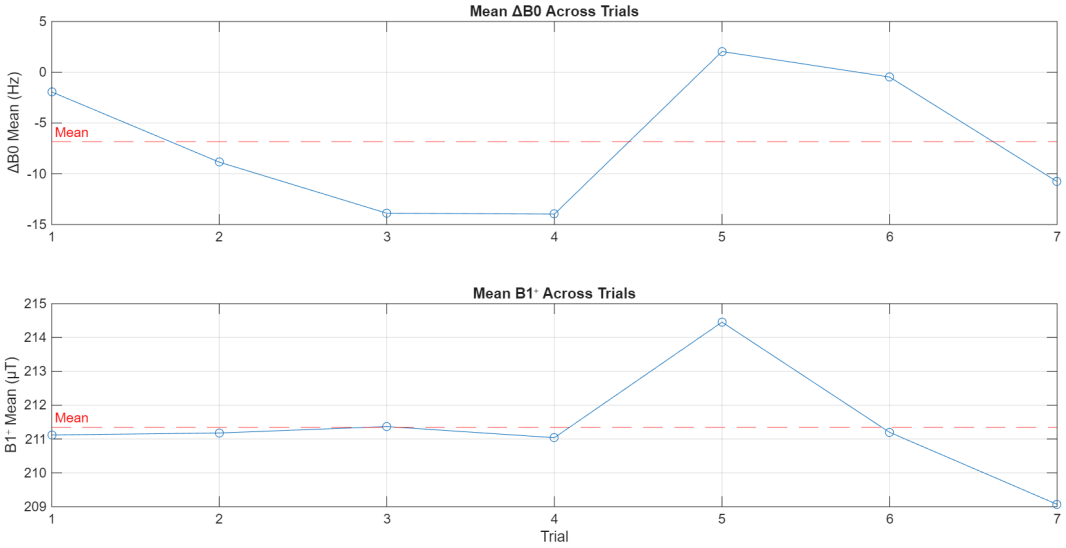

Figure 5.8: Mean of ΔB_0 and B_1^+ across 7 trials, indicating scanner stability

across trials suggests that their influence on the results would have been negligible. Given the high stability of both fields, additional correction steps were unlikely to meaningfully affect the repeatability outcomes.

To further evaluate scanner stability, the SNR was calculated across all trials using the b = 0 image from the DTI acquisition. SNR was estimated as the ratio of mean signal intensity within the phantom to the standard deviation of signal within a background ROI (Figure 5.9).

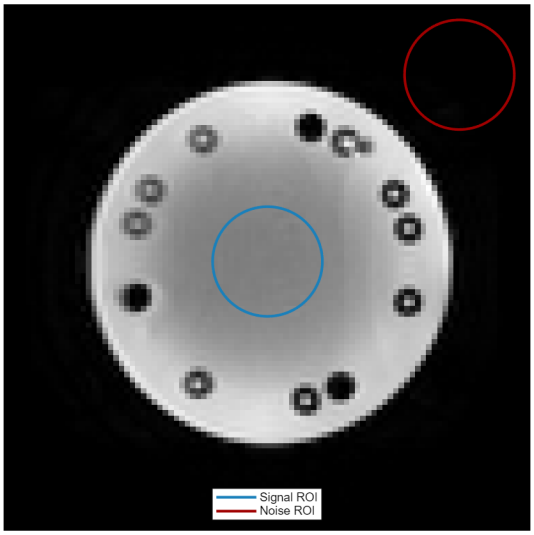

Figure 5.9: Example ROI placement for SNR calculation using a central slice of the b = 0 image.

Across the 11 trials, the mean SNR was 97.83 with a standard deviation of 7.03 (Figure 5.10). This low variability in SNR further supports the consistency of scanner performance and shows that observed changes in diffusion metrics are unlikely to be driven by noise-related fluctuations. Stable SNR values indicate that RF excitation, coil loading, and overall system performance remained consistent throughout the repeated scans.

To provide a baseline repeatability estimate, ADC values were calculated from the

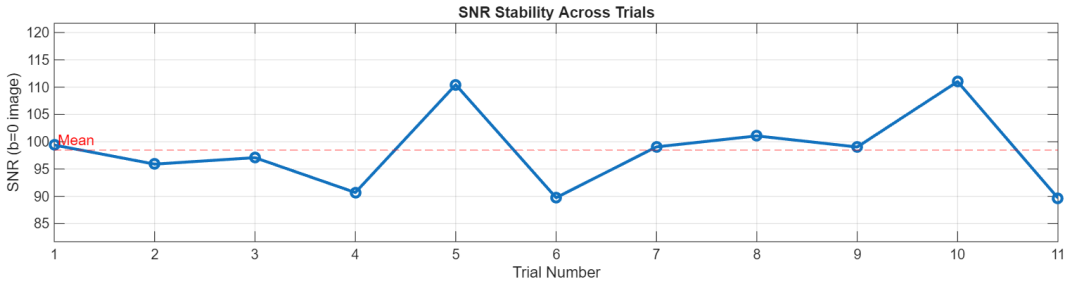

Figure 5.10: Trial-wise SNR measurements across all 11 scans demonstrating consistency in signal quality.

PROPELLER DWI scan at the 1200 $\times 10^{-6}$ mm^2/s isotropic diffusion module. This region is designed to have stable and known diffusivity and does not contain any fibre structures. Across all 11 trials, the mean ADC was 1227×10^{-6} mm^2/s, the SD was 22.48×10^{-6} mm^2/s, and the CoV was 1.83%.

Taken together, the uniformity of the ΔB_0 and B_1^+ maps, the stability of the SNR, and the low CoV in ADC measurements demonstrates that scanner performance remained consistent over the imaging sessions. These results suggest that any observed variability in diffusion metrics likely reflects model or fibre effects, rather than hardware instability.

Chapter 6

Discussion and Conclusion

6.1 Summary of Key Findings

This study evaluated the repeatability of advanced dMRI metrics using a novel anisotropic phantom developed by PreOperative Performance. Across 11 independent scan sessions, metrics were derived from DTI, DKI, and CSD models and assessed in six distinct ROIs with varying fibre geometries. Repeatability was quantified using the CoV and ICC.

In general, DTI-derived metrics showed high repeatability across all ROIs and scanning protocols. FA exhibited CoVs <10% while MD, AD, and RD had CoVs <3%. The overall trend was that CoV decreased and ICC increased when using HARDI acquisitions. All ICC values for FA, MD, and RD showed excellent reliability between scans (ICC>0.9), with AD showing only good reliability (although only missing the threshold for excellent reliability by 0.0043 for the HARDI-90 protocol).

DKI metrics displayed greater variability than their DTI analogs. KFA showed low CoV (4–11%) and maintained strong ICCs. MK values ranged widely in CoV

(10–27%), with the highest variability in ROIs featuring fibre crossings or branching. AK and RK had the least stability, with CoV exceeding 30% in certain ROIs. Despite a higher CoV, KFA and AK were still classified as having excellent reliability according to their ICC values compared to MK and RK, which demonstrated only good reliability.

GFA showed a clear increase in reliability with higher angular resolution, as ICCs were 0.6603 (DTI), 0.8046 (HARDI-60), and 0.8507 (HARDI-90). This improvement in ICC reflects better differentiation between ROIs and reduced variability across trials. In comparison, CoV remained relatively low, even with only 30 gradient directions. Together, these results indicate that the HARDI protocols enable better discrimination between distinct fibre geometries, likely due to more accurate estimation of the fODF in complex regions. GFA results do show repeatability between scanning sessions, but the low ICC may be due to crossing fibres being consistently misrepresented by the CSD model.

6.2 ROI-Specific Observations

Overall, DTI metrics demonstrate high repeatability, with some effects that can be attributed to fibre geometry (Tables 5.1–5.5). For FA, it was noted that ROI 2 has the highest mean value, potentially due to the narrow 30° crossing angle leading to overlapping diffusion orientations and an artificially elevated principal axis. In contrast, ROI 4 (90° intersection) had a lower FA, which could be the result of a more oblate tensor shape and diminished anisotropy. This is also supported by ROI 4 having the lowest AD among complex geometry locations, since diffusion would be suppressed along the principal axis. ROIs 1 and 3 (45° crossing and fibre branching)

show intermediate FA values, with ROI 3 showing higher variability, possibly related to the out-of-plane component of the third branch. ROI 5, a simple linear fibre, had the highest AD and showed consistently low CoV, reinforcing that its single-direction architecture aligned well with the model's assumptions. ROI 6, the isotropic region, served as a low variance benchmark and behaved as expected.

DKI metrics showed higher variability across ROIs, especially MK, AK, and RK (Tables 5.6–5.7). KFA, being a normalized metric, offered the most consistent trends. ROI 5, despite being structurally simple, exhibited the most variable values and highest CoV. One plausible explanation could be inconsistencies in fibre packing or effects of noise being amplified at this location. As expected, ROI 6, which contains no fibres, showed very low kurtosis values. This confirms that the Gaussian diffusion assumption holds well in isotropic regions, and the kurtosis model correctly reflects minimal microstructural complexity. In the complex geometry fibres, no obvious trends emerged. For example, KFA remained relatively stable, but AK and RK varied non-linearly across different geometries. This may be due to the relationship between fibre structure and kurtosis being much more nuanced.

CSD-derived GFA provided clear geometric differentiation, with the strongest directional anisotropy observed in ROIs 1–4 (Tables 5.8–5.9). GFA increased with angular resolution, and the differences between ROIs became more apparent in the HARDI-90 acquisition. For example, ROI 4, containing a 90° fibre crossing, showed the highest GFA in the HARDI-90 data, likely because orthogonal bundles yield distinct lobes in the fODF that improve angular contrast. ROI 2 showed lower GFA despite its crossing design, which is consistent with the fODF visualizations where the 30 ° crossing was not resolved as two peaks. ROI 3 exhibited moderate GFA

values, again reflecting the complexity of its three-branch configuration. In isotropic ROI 6, GFA was consistently near zero, validating that the model appropriately captured the absence of directional preference. The linear ROI (ROI 5) had low but stable GFA, aligning with the expectation that a single coherent direction yields a compact fODF with moderate anisotropy.

Qualitative visualization of the fODF peaks provided important insights into CSD model performance (Figures 5.1–5.6). In ROI 1, the detected crossing angle (49.8°) was close to the expected 45°, confirming accurate angular resolution at moderate intersection angles. ROI 3 successfully revealed three distinct fibre directions, including an out-of-plane branch. ROI 4 showed two orthogonal peaks (84.6°), closely matching the expected 90°, while ROI 5 and ROI 6 behaved as expected for linear and isotropic regions, respectively. ROI 2 showed only a single peak despite a known 30° crossing, reflecting a well-documented limitation of CSD in resolving shallow fibre angles. These results complement the GFA trends and reinforce the importance of high angular resolution and careful interpretation in orientation-resolved diffusion modelling.

6.3 Comparison to Prior Phantom Studies

The repeatability results of this study align well with findings from earlier diffusion MRI phantom research, particularly those using anisotropic models designed to simulate white matter microstructure. As summarized in the literature review (Table 3.1), prior studies generally report low coefficients of variation (CoV) for standard DTI metrics, with FA CoVs often below 5% in stable, linear fibre modules. This study found similar trends, with average FA CoVs ∼9% and even lower CoVs (<3%)

for MD, AD, and RD, especially under HARDI acquisitions.

These values are well within the variability ranges reported by studies using synthetic fibre phantoms like those by Teipel et al., Hakulinen et al., and de Souza et al., further supporting the phantom's use as a reliable QA tool for DTI validation [60, 61, 64]. However, this work extends the current literature by comprehensively evaluating higher-order diffusion models. While a few recent studies (e.g., Kasa et al. and Mushtaha et al.) reported reproducibility for DKI metrics, they often focused on only a subset of scalar measures or simpler fibre configurations. In contrast, this study examined four DKI-derived metrics (MK, AK, RK, and KFA) across multiple complex fibre geometries [66, 67].

Simard et al. conducted a reproducibility assessment using an earlier version of the same PreOperative Performance phantom, focusing exclusively on DTI metrics (FA, MD, AD, RD) acquired across three different vendors and various motion probing gradient schemes [14]. The phantom used previously included only bifurcating and orthogonal fibre modules, whereas the version used in this study (POP-0005-001) incorporates a broader range of fibre geometries, including acute angle crossings and fibre branching. Simard et al. found no statistically significant differences in diffusion metrics across vendor platforms or motion probing gradient tables. This benchmarked the phantom as a robust standard for evaluating inter-scanner and inter-vendor reproducibility in DTI. The present study complements and extends these findings by evaluating intra-scanner repeatability and by including advanced diffusion models.

6.4 Limitations

6.4.1 Sample Size

One limitation of this study is the relatively small number of repeated trials (n = 11) used to assess repeatability. While a larger number of scans could provide even more robust estimates, the chosen sample size is supported both by statistical reasoning and precedent in the literature. A key consideration in reproducibility studies is how many repeated measurements are needed to reliably estimate the ICC. Walter, Eliasziw, and Donner present an approach to sample size planning for studies that use the ICC as a measure of reliability [68]. This method is based on hypothesis testing, which aims to determine the number of subjects required to reject a null hypothesis of "unacceptable" reliability in favour of a higher, "acceptable" target reliability.

We suppose that n observations (in this case, scans) are made of k subjects (in this case, ROIS). The method assumes a two-way ANOVA model and provides a formula to calculate the minimum number of ROIs needed:

$$k = 1 + \frac{2(Z_\alpha + Z_\beta)^2 n}{(\ln C_0)^2 (n-1)} \tag{6.4.1}$$

where:

$$C_0 = \frac{1 + n(\frac{\rho_0}{1-\rho_0})}{1 + n(\frac{\rho_1}{1-\rho_1})} \tag{6.4.2}$$

and:

- k is the number of ROIs needed
- n is the number of observations per ROI (scans)
- ρ_0 is the null ICC (e.g. 0.6)

- ρ_1 is the alternative ICC (e.g. 0.9)
- $\alpha = 0.05$ (type I error)
- $\beta = 0.2$ (for 80% power)

Since the number of ROIs ($k = 6$) was fixed in the study, the equation was solved iteratively to determine the minimum number of trials required to detect a difference between $\rho_0 = 0.6$ and $\rho_1 = 0.9$. The result showed that only 7 trials were needed, confirming that the chosen design with 11 trials provides more than sufficient power to support the repeatability analysis performed. As such, the high ICC values observed across all ROIs are unlikely to be due to random chance or sampling variability.

In addition to statistical justification, the number of repeated trials used in this study is supported by precedent in the diffusion MRI phantom literature. Many previous reproducibility studies have used substantially fewer repeated scans. For example, Wilde et al. scanned 8 times across 4 different sites [62] and Provenzale et al. used 7 total scans (4 on one scanner and 3 on another) [63]. Teipel et al. used 8 scans across 8 different sites [60] and Grech-Sollars et al. scanned 8 times across 5 different sites [69], both evaluating multicentre reproducibility. These examples demonstrate that the use of 11 repeated scans in the present study not only meets but exceeds the level of repetition commonly employed in diffusion MRI phantom reproducibility research.

6.4.2 Scanning Methodology

Although the scanner remained stable across sessions, as verified by ΔB_0, B_1^+, SNR, and ADC consistency, several practical limitations remain. All scans were conducted on a single 3.0T GE scanner at a single site, using the same protocols, coil, and

operator workflows. As such, the results should be interpreted as intra-scanner, intra-protocol repeatability. While this ensures internal consistency, it limits the generalizability of results to other scanner models, vendors, or field strengths. Future work would benefit from multi-centre data collection to assess inter-site and inter-vendor variability. Second, while the phantom was repositioned between trials, the lack of strict repositioning control (e.g., using a rigid holding structure) could introduce minor alignment differences. Although affine registration was applied during postprocessing, residual misalignment could still affect voxel-wise comparisons. While the 3×3×3 voxel box design reduces sensitivity to registration noise, it also inevitably includes some non-fibre isotropic voxels within the average.

6.4.3 Metric Interpretation

CoV and ICC, while widely used to quantify repeatability, have their own assumptions and weaknesses. CoV is sensitive to the absolute scale of the metric, meaning that low-magnitude values can appear highly variable even if the absolute change is small (as seen in RK and MK). ICC depends heavily on between-subject variability, so models that blur regional distinctions (e.g., due to poor angular resolution) may show lower ICC even if they are stable within each ROI (as discussed with GFA).

Additionally, repeatability metrics do not reflect accuracy, as a highly repeatable model can consistently misrepresent the truth. Without ground truth measurements, the absolute error of each model remains unknown. This limits the ability to interpret whether variability is due to model limitations, measurement noise, or actual differences in the phantom structure.

6.5 Future Work

The current study was intentionally limited to a single scanner and a fixed phantom geometry to isolate model-specific effects. However, extending the scope to assess inter-scanner and inter-vendor variability is a natural next step. MRI vendors attempt to harmonize acquisition protocols across platforms, but meaningful differences remain in gradient hardware, diffusion encoding schemes, RF coil designs, and image reconstruction algorithms. Including scanners from multiple vendors (i.e. Siemens, Philips, etc.) would allow for a more comprehensive evaluation of reproducibility across imaging systems and could inform the development of vendor-agnostic QA standards.

In addition to scanner diversity, future studies would benefit from evaluating multiple PreOperative Performance phantoms with different internal configurations. The phantom used in this study contained a representative set of fibre geometries, but expanding this to include more complex features (curvilinear tracts or fibre density gradients) would test the limits of each model's ability to resolve microstructural variation.

Another important factor warranting systematic investigation is temperature dependence. Diffusion metrics are intrinsically temperature-sensitive (since rate of diffusion is dependent on temperature). In this study, the phantom was scanned under controlled room-temperature conditions, but small deviations in thermal equilibrium may influence diffusivity and kurtosis estimates. For multisite studies, room temperature may fluctuate by several degrees, so characterizing the effect of ambient temperature could help guide best practices for using the phantom.

6.6 Conclusions

This study demonstrated that the PreOperative Performance anisotropic phantom is a reliable and effective tool for evaluating the repeatability of advanced diffusion MRI metrics. Despite differences in model assumptions and sensitivities, the phantom supported consistent measurements across a range of fibre geometries, particularly under high angular resolution acquisitions. As advanced diffusion imaging continues to expand in clinical and research settings, standardized physical phantoms like this one will be essential for quality assurance, protocol optimization, and cross-site harmonization. Overall, this work establishes the phantom as a practical benchmark for diffusion metric stability and provides a foundation for future reproducibility studies across scanners, vendors, and acquisition strategies.

Appendix A

Data Analysis Code

A.1 Required Imports

```
import os
import numpy as np
import nibabel as nib
import cv2
import pandas as pd
from dipy.io.image import load_nifti
from dipy.io.gradients import read_bvals_bvecs
from dipy.core.gradients import gradient_table
from dipy.reconst.dti import TensorModel
from dipy.reconst.dki import DiffusionKurtosisModel
from dipy.reconst.csdeconv import auto_response_ssst,
    ConstrainedSphericalDeconvModel
from dipy.denoise.localpca import mppca
from scipy.ndimage import label, binary_fill_holes
from pingouin import intraclass_corr
```

Listing A.1: Required imports for the following functions.

A.2 Preprocessing

```
def load_diffusion_data(data_dir):
    """
    Load diffusion MRI data from multiple trials within a directory.

    Parameters:
    data_dir (str): Path to the directory containing trial folders.

```

```
    Returns:
    datasets {dict}: A dictionary containing loaded data categorized
        by imaging type.
    """

    datasets = {
        "T1": [],
        "DWI": [],
        "DTI": [],
        "HARDI_60": [],
        "HARDI_90": [],
        "DKI": []
    }

    scan_types = {
        "T1": "20_FSPGR_3D_1mm_ISO",
        "DWI": "30_DWI_PROPELLER_3",
        "DTI": "40_DTI_30",
        "HARDI_60": "50_HARDI_60",
        "HARDI_90": "60_HARDI_90",
        "DKI": "70_DKI_30"
    }

    for trial_folder in os.listdir(data_dir):

        if trial_folder in ["masks", "transforms"]:
            continue

        trial_path = os.path.join(data_dir, trial_folder)

        if not os.path.isdir(trial_path):
            continue

        for scan_type, file_prefix in scan_types.items():
            data_file = os.path.join(trial_path, f"{file_prefix}.nii
                ")
            bvals_file = os.path.join(trial_path, f"{file_prefix}.
                bval")
            bvecs_file = os.path.join(trial_path, f"{file_prefix}.
                bvec")

            try:
                if scan_type == "T1":
                    data, affine = load_nifti(data_file)
                    datasets[scan_type].append((data, affine))
                else:
                    data, affine = load_nifti(data_file)
                    bvals, bvecs = read_bvals_bvecs(bvals_file,
                        bvecs_file)
                    gtab = gradient_table(bvals, bvecs) if scan_type
                         != "DWI" else None
                    datasets[scan_type].append((data, affine, gtab)
                        if gtab else (data, affine))
            except FileNotFoundError:
```

```
                print(f"No file found: {data_file}")

    return datasets
```

Listing A.2: Function to load dMRI scans and gradient tables from all trials into a structured dataset.

```
def process_mask(binary_mask):

    """
    Removes holes and background noise from a thresholded phantom
        mask.

    Parameters:
    binary_mask (array): Binary mask file that holds the thresholded
         phantom mask.

    Returns:
    final_mask (array): A processed binary mask file with holes and
        noise removed.
    """

    # Fill holes using morphological closing and flood filling
    kernel = np.ones((9, 9), np.uint8)
    closed_mask = cv2.morphologyEx(binary_mask.astype(np.uint8), cv2
        .MORPH_CLOSE, kernel)
    final_mask = binary_fill_holes(closed_mask).astype(np.uint8)

    # Keep only the largest connected component
    labeled_array, num_features = label(final_mask)

    if num_features > 1:
        largest_component = np.argmax(np.bincount(labeled_array.flat
            )[1:]) + 1
        final_mask = (labeled_array == largest_component).astype(np.
            uint8)

    return final_mask
```

Listing A.3: Function to create binary masks by removing holes and retaining the largest connected component.

```
def denoise_mppca(scan_type):

    """
    Apply MPPCA denoising to DTI, HARDI_60, HARDI_90, and DKI data
        in the datasets dictionary.

    Parameters:
    scan_type (str): String that corresponds to the dataset
        dictionary category.

```

```
    """

    for i, (data, affine, gtab) in enumerate(datasets[scan_type]):
        mask = masks[i]
        denoised_data = mppca(data, mask=mask)
        datasets[scan_type][i] = (denoised_data, affine, gtab)

        print(f"Denoised entry {i + 1}")
```

Listing A.4: Applies MP-PCA denoising to diffusion datasets.

A.3 Modelling

```
def fit_tensor_model(scan_type):

    """
    Fits the DiPy TensorModel to the data

    Parameters:
    scan_type (str): String that corresponds to the dataset
       dictionary category

    Returns:
    model (array): An array holding the fitted models for each trial
       .
    affine_list (array): An array holding the affine transformations
        for each trial.
    """

    model = []
    affine_list = []

    for i, (data, affine, gtab) in enumerate(datasets[scan_type]):

        print("Processing " + str(scan_type) + f" dataset {i+1}")

        N = data.shape[3]
        mask = masks[i]
        mask_full = np.repeat(mask[:, :, :, np.newaxis], N, axis=3)

        data = data * mask_full

        ten_model = TensorModel(gtab)
        ten_fit = ten_model.fit(data, mask=mask)

        model.append(ten_fit)
        affine_list.append(affine)

    return model, affine_list
```

Listing A.5: Fits a diffusion tensor model (DTI) to masked diffusion data using DiPy's *TensorModel* class.

```
def fit_kurtosis_model(scan_type):
    """
    Fits the DiPy DiffusionKurtosisModel to the data

    Parameters:
    scan_type (str): String that corresponds to the dataset
       dictionary category

    Returns:
    model (array): An array holding the fitted models for each trial
       .
    affine_list (array): An array holding the affine transformations
        for each trial.
    """

    model = []
    affine_list = []

    for i, (data, affine, gtab) in enumerate(datasets[scan_type]):

        print("Processing " + str(scan_type) + f" dataset {i+1}")

        N = data.shape[3]
        mask = masks[i]
        mask_full = np.repeat(mask[:, :, :, np.newaxis], N, axis=3)

        data = data * mask_full

        dki_model = dki.DiffusionKurtosisModel(gtab)
        dki_fit = dki_model.fit(data, mask=mask)

        model.append(dki_fit)
        affine_list.append(affine)

    return model, affine_list
```

Listing A.6: Fits a diffusion kurtosis model to masked data using DiPy's *DiffusionKurtosisModel* class.

```
def get_CSD_model(scan_type):

    """
    Estimates the response function and constructs the CSD model.

    Parameters:
    scan_type (str): String that corresponds to the dataset
       dictionary category.
```

```
8
9       Returns:
10      model_fit (list): List holding unfitted CSD models for each
            trial.
11      """
12
13      model_fit = []
14
15      for i, (data, affine, gtab) in enumerate(datasets[scan_type]):
16
17          print("Processing␣" + str(scan_type) + f"␣dataset␣{i+1}")
18
19          roi = [54, 46, 54]
20          roi_radius = 4
21          lmax = 8
22
23          response, ratio = auto_response_ssst(gtab, data, roi_center
                = roi, roi_radii = roi_radius, fa_thr = 0.7)
24
25          csd_model = ConstrainedSphericalDeconvModel(gtab, response,
                sh_order_max=lmax)
26
27          model_fit.append(csd_model)
28
29      return model_fit
30
31  def fit_CSD_model(scan_type, model_list):
32
33      """
34      Fits the CSD model to each trial in the dataset.
35
36      Parameters:
37      scan_type (str): String that corresponds to the dataset
            dictionary category.
38      model_list (list): List holding CSD models for each trial.
39
40      Returns:
41      computed_CSD (list): List holding fitted CSD results for each
            trial.
42      """
43
44      computed_CSD = []
45
46      for i, (csd_model) in enumerate(model_list):
47
48          data = datasets[scan_type][i][0]
49
50          csd_fit = csd_model.fit(data)
51
52          computed_CSD.append(csd_fit)
53
54      return computed_CSD
```

Listing A.7: Estimates the response function and fits the constrained spherical deconvolution model using DiPy's *ConstrainedSphericalDeconvModel*.

A.4 Postprocessing

```
def get_FA(scan_type, model_list, affine_list, optional_save = 0):

    """
    Saves the DiPy TensorModel FA maps to compute transformation
       matrix.

    Parameters:
    scan_type (str): String that corresponds to the dataset
       dictionary category.
    model_list [list]: List that holds TensorModels for the
       different trials.
    affine_list [list]: List that holds the affine transformations
       for the different trials.
    optional_save (int, optional): If set to 1, the FA maps will be
       saved to computer. If 0, the function will compute but not
       save the FA maps. Defaults to 0.

    Returns:
    FA_list [list]: List that holds FA maps as Nifti images for the
       different trials.
    """

    FA_list = []

    for i, (model) in enumerate(model_list):

        FA = model.fa
        FA_list.append(FA)

        if optional_save == 1:
            FA_nifti = nib.Nifti1Image(FA, affine_list[i])
            filename = scan_type + f"FA_map_{i+1}.nii.gz"
            nib.save(FA_nifti, filename)


    return FA_list
```

Listing A.8: Extracts and optionally saves FA maps from tensor model fits. Other functions exist for computing other scalar metrics that follow the same general structure.

```
def get_ROI_values(scan_data, ROIs, box_size=(3, 3, 3)):
    """
```

```
    Extracts 3D ROI values and computes their mean across scans.

    Parameters:
    scan_data (list): List of 3D or 4D scan arrays for each trial.
    ROIs (list): List of (x, y, z) voxel coordinates for each ROI.
    box_size (tuple): Size of the cubic ROI, default is (3, 3, 3).

    Returns:
    result (list): List of flattened voxel values for each ROI and
        scan.
    avg (list): List of mean values for each ROI and scan.
    """

    x_box, y_box, z_box = box_size
    result = []
    avg = []

    for i, roi in enumerate(ROIs):
        x, y, z = roi
        trial_result = []
        trial_averages = []

        for scan in scan_data:
            # Define the bounding box for the ROI
            x_min = max(0, x - x_box // 2)
            x_max = min(scan.shape[0], x + x_box // 2 + 1)
            y_min = max(0, y - y_box // 2)
            y_max = min(scan.shape[1], y + y_box // 2 + 1)
            z_min = max(0, z - z_box // 2)
            z_max = min(scan.shape[2], z + z_box // 2 + 1)

            # Extract the 3D box
            roi_values = scan[x_min:x_max, y_min:y_max, z_min:z_max]

            # Remove outliers (values > 1) before computing mean

            roi_values_filtered = np.where(roi_values < 1,
                roi_values, np.nan)
            trial_result.append(roi_values_filtered.flatten())

            # Compute the mean only on valid values
            roi_avg = np.mean(roi_values_filtered) if
                roi_values_filtered.size > 0 else np.nan

            trial_averages.append(roi_avg)

        result.append(trial_result)
        avg.append(trial_averages)

    return result, avg
```

Listing A.9: Extracts voxel-wise scalar values from 3D ROI cubes across all trials.

```
def stat_analysis (values, averages):

    """
   Computes repeatability statistics for each ROI.

   Parameters:
   values (list): Nested list of voxel values per ROI and scan.
   averages (list): Nested list of mean values per ROI and scan.

   Prints:
   - Mean, standard deviation, min, max, and CoV for each ROI.
   - Average CoV across all ROIs.
   - Intraclass correlation coefficient (ICC) for scan consistency.
   """

    values = np.array(values)

    averages = np.array(averages)  # Convert to NumPy array for easy operations
    num_rois, num_scans = averages.shape

    print("\n=== Statistical Analysis of ROI Values Across Scans ===\n")

    cov_sum = 0

    for i in range(num_rois):

        roi_values = averages[i, :]
        mean_val = np.nanmean(roi_values)
        std_dev = np.nanstd(roi_values)
        min_val, max_val = np.nanmin(roi_values), np.nanmax(roi_values)
        coef_var = std_dev / mean_val if mean_val != 0 else np.nan

        print(f"ROI {i + 1}:")
        print(f"  Mean: {mean_val:.4f}")
        print(f"  Standard Deviation: {std_dev:.4f}")
        print(f"  Min: {min_val:.4f}, Max: {max_val:.4f}")
        print(f"  Coefficient of Variation (CV): {coef_var:.4f}")
        print("\n")

        cov_sum += coef_var

        avg_cov = cov_sum/6

    print(f"  Average CoV: {avg_cov:.4f}")

    print("\n=== Intraclass Correlation Coefficient (ICC) for Scan Consistency ===\n")

    # Convert values to long-format DataFrame for ICC calculation
    scan_labels = np.tile(np.arange(1, num_scans + 1), num_rois)
```

```
    roi_labels = np.repeat(np.arange(1, num_rois + 1), num_scans)
    flattened_values = averages.flatten()

    df_icc = pd.DataFrame({
        "Scan": scan_labels,
        "ROI": roi_labels,
        "Value": flattened_values
    })

    icc_results = intraclass_corr(data=df_icc, targets="ROI", raters
       ="Scan", ratings="Value", nan_policy='omit')
    icc_val = icc_results.loc[icc_results["Type"] == "ICC3", "ICC"].
       values[0]

    print(f"  ICC: {icc_val:.4f}")
```

Listing A.10: Performs repeatability statistics on ROI data, including mean, standard deviation, coefficient of variation, and ICC.

Appendix B

Supplemental Data

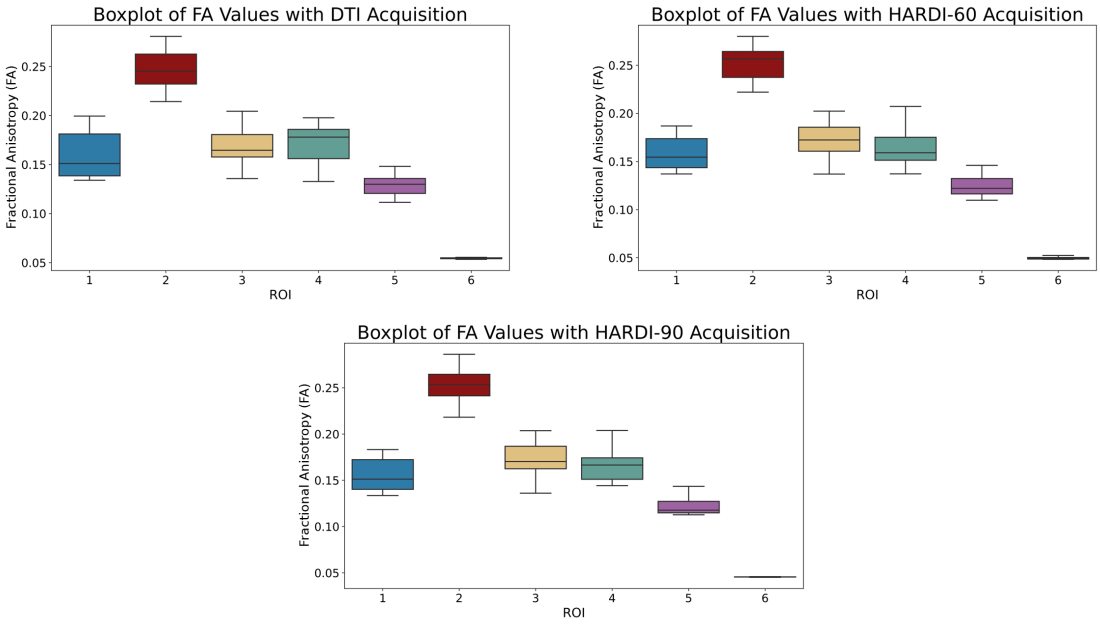

Figure B.1: Boxplots of FA values across ROIs and scanning protocols

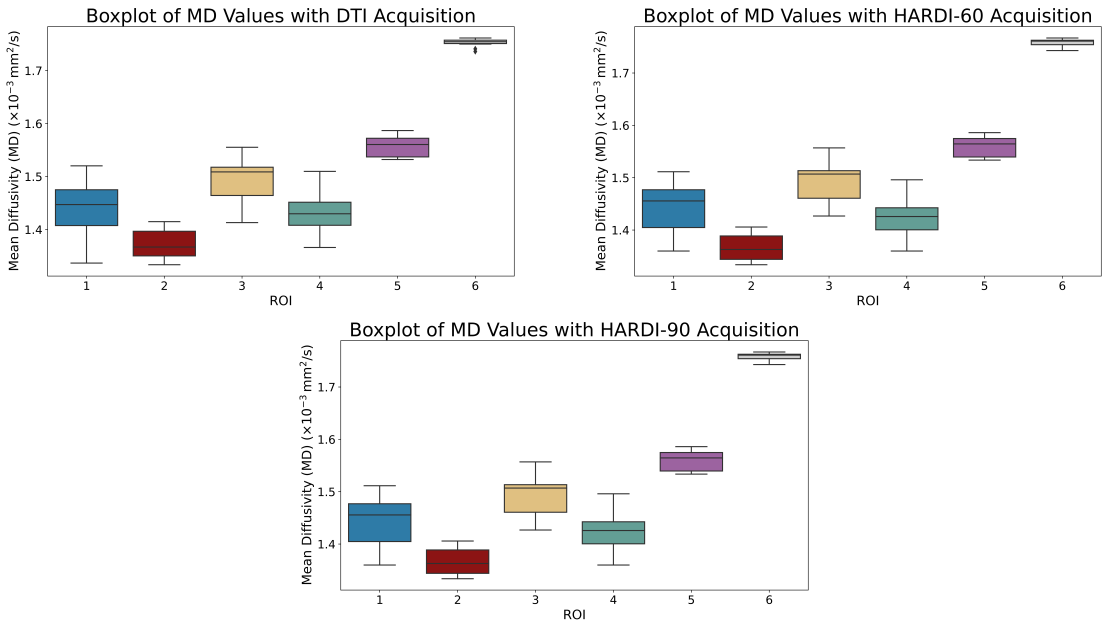

Figure B.2: Boxplots of MD values across ROIs and scanning protocols

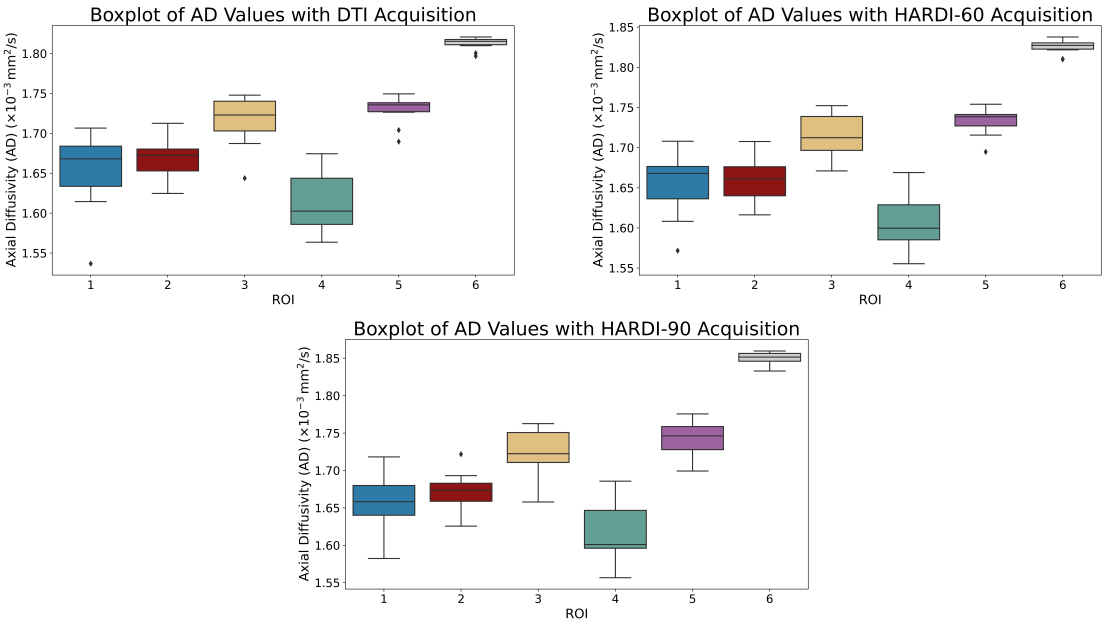

Figure B.3: Boxplots of AD values across ROIs and scanning protocols

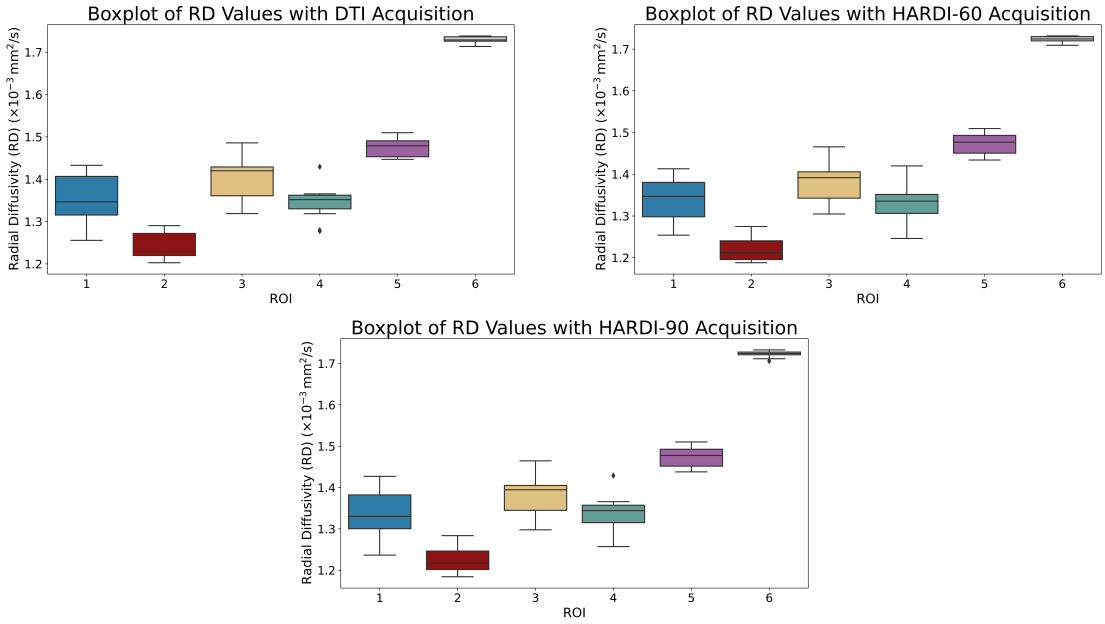

Figure B.4: Boxplots of RD values across ROIs and scanning protocols

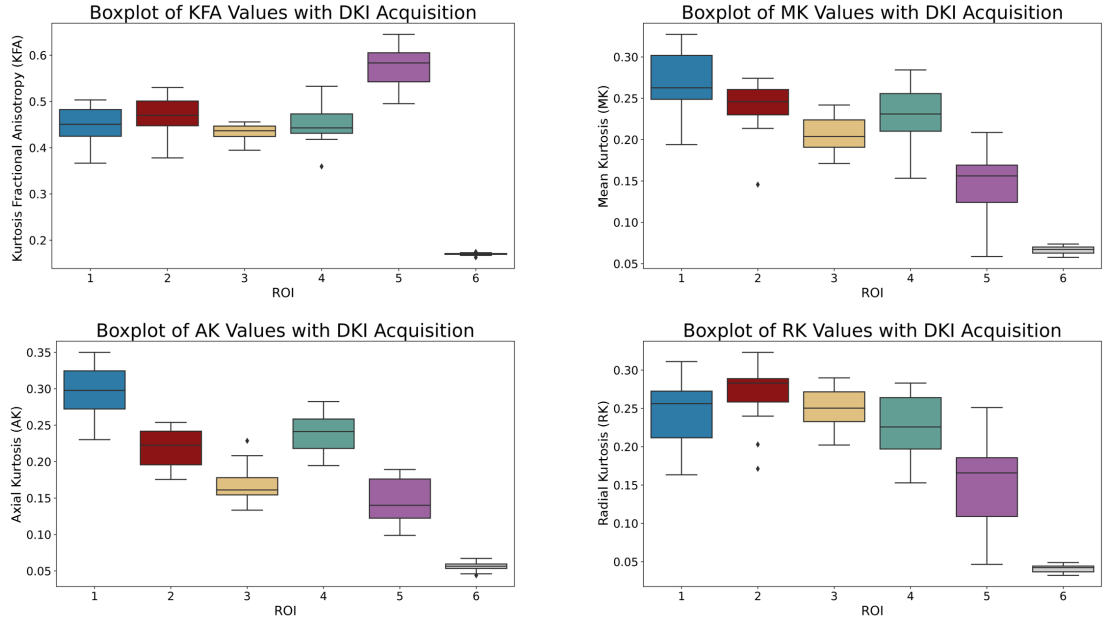

Figure B.5: Boxplots of kurtosis-derived metrics across ROIs

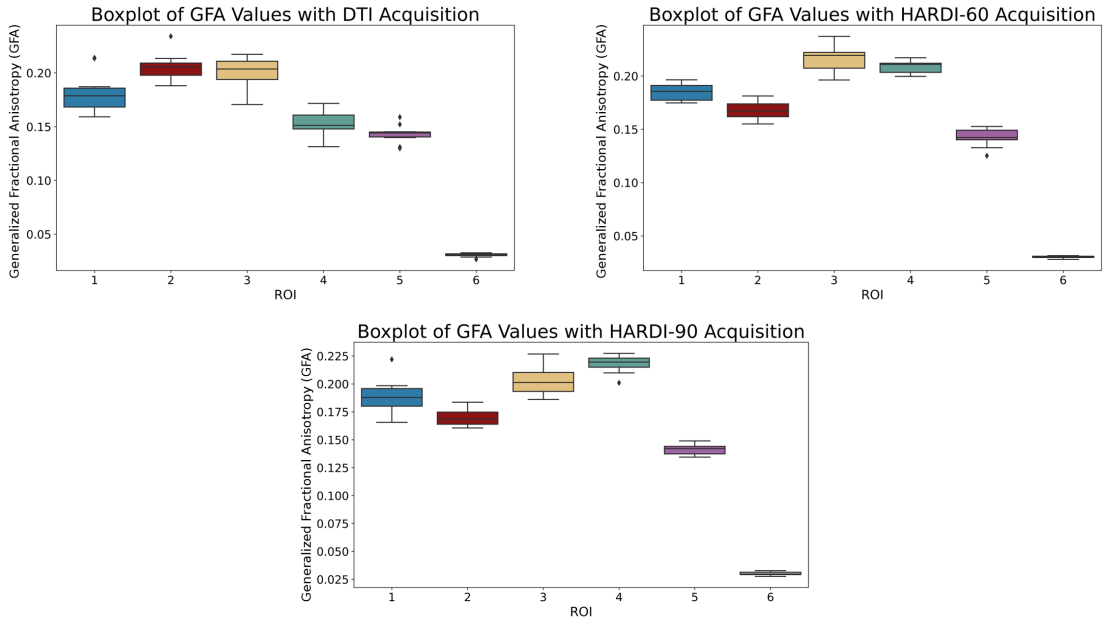

Figure B.6: Boxplots of GFA values across ROIs and scanning protocols

Bibliography

[1] C. Rosso, O. Colliot, C. Pires, C. Delmaire, R. Valabrègue, S. Crozier, D. Dormont, S. Baillet, Y. Samson, and S. Lehéricy, "Early ADC changes in motor structures predict outcome of acute stroke better than lesion volume," *Journal of Neuroradiology*, vol. 38, no. 2, pp. 105–112, May 2011. [Online]. Available: https://www.sciencedirect.com/science/article/pii/S0150986110001057

[2] B. Kim, B. E. Fisher, N. Schweighofer, R. M. Leahy, J. P. Haldar, S. Choi, D. B. Kay, J. Gordon, and C. J. Winstein, "A comparison of seven different DTI-derived estimates of corticospinal tract structural characteristics in chronic stroke survivors," *Journal of Neuroscience Methods*, vol. 304, pp. 66–75, Jul. 2018. [Online]. Available: https://www.sciencedirect.com/science/article/pii/S0165027018301134

[3] E. L. Yuh, S. R. Cooper, P. Mukherjee, J. K. Yue, H. F. Lingsma, W. A. Gordon, A. B. Valadka, D. O. Okonkwo, D. M. Schnyer, M. J. Vassar, A. I. Maas, G. T. Manley, and the TRACK-TBI INVESTIGATORS including, S. S. Casey, M. Cheong, K. Dams-O'Connor, A. J. Hricik, T. Inoue, D. K. Menon, D. J. Morabito, J. L. Pacheco, A. M. Puccio, and T. K. Sinha, "Diffusion

Tensor Imaging for Outcome Prediction in Mild Traumatic Brain Injury: A TRACK-TBI Study," *Journal of Neurotrauma*, vol. 31, no. 17, pp. 1457–1477, Sep. 2014, publisher: Mary Ann Liebert, Inc., publishers. [Online]. Available: https://www.liebertpub.com/doi/10.1089/neu.2013.3171

[4] S. M. Mustafi, J. Harezlak, C. Kodiweera, J. S. Randolph, J. C. Ford, H. A. Wishart, and Y.-C. Wu, "Detecting white matter alterations in multiple sclerosis using advanced diffusion magnetic resonance imaging," *Neural Regeneration Research*, vol. 14, no. 1, p. 114, Jan. 2019. [Online]. Available: https://journals.lww.com/nrronline/fulltext/2019/14010/Detecting_white_matter_alterations_in_multiple.24.aspx

[5] N. Spotorno, O. Strandberg, E. Stomrud, S. Janelidze, K. Blennow, M. Nilsson, D. van Westen, and O. Hansson, "Diffusion MRI tracks cortical microstructural changes during the early stages of Alzheimer's disease," *Brain*, vol. 147, no. 3, pp. 961–969, Dec. 2023, _eprint: https://academic.oup.com/brain/article-pdf/147/3/961/56816930/awad428.pdf. [Online]. Available: https://doi.org/10.1093/brain/awad428

[6] T. E. J. Behrens, H. J. Berg, S. Jbabdi, M. F. S. Rushworth, and M. W. Woolrich, "Probabilistic diffusion tractography with multiple fibre orientations: What can we gain?" *NeuroImage*, vol. 34, no. 1, pp. 144–155, Jan. 2007.

[7] B. Jeurissen, A. Leemans, J. Tournier, D. K. Jones, and J. Sijbers, "Investigating the prevalence of complex fiber configurations in white matter tissue with diffusion magnetic resonance imaging," *Human Brain*

Mapping, vol. 34, no. 11, pp. 2747–2766, May 2012. [Online]. Available: https://www.ncbi.nlm.nih.gov/pmc/articles/PMC6870534/

[8] D. A. Raffelt, J. D. Tournier, R. E. Smith, D. N. Vaughan, G. Jackson, G. R. Ridgway, and A. Connelly, "Investigating white matter fibre density and morphology using fixel-based analysis," *NeuroImage*, vol. 144, pp. 58–73, Jan. 2017. [Online]. Available: https://www.sciencedirect.com/science/article/pii/S1053811916304943

[9] S. B. Vos, C. M. W. Tax, P. R. Luijten, S. Ourselin, A. Leemans, and M. Froeling, "The importance of correcting for signal drift in diffusion MRI," *Magnetic Resonance in Medicine*, vol. 77, no. 1, pp. 285–299, Jan. 2017.

[10] E. Palacios, A. Martin, M. Boss, F. Ezekiel, Y. Chang, E. Yuh, M. Vassar, D. Schnyer, C. MacDonald, K. Crawford, A. Irimia, A. Toga, and P. Mukherjee, "Toward Precision and Reproducibility of Diffusion Tensor Imaging: A Multicenter Diffusion Phantom and Traveling Volunteer Study," *American Journal of Neuroradiology*, vol. 38, no. 3, pp. 537–545, Mar. 2017. [Online]. Available: http://www.ajnr.org/lookup/doi/10.3174/ajnr.A5025

[11] Z. J. Wang, Y. Seo, E. Babcock, H. Huang, S. Bluml, J. Wisnowski, B. Holshouser, A. Panigrahy, D. W. Shaw, N. Altman, R. W. McColl, and N. K. Rollins, "Assessment of diffusion tensor image quality across sites and vendors using the American College of Radiology head phantom," *Journal of Applied Clinical Medical Physics*, vol. 17, no. 3, pp. 442–451, May 2016. [Online]. Available: https://www.ncbi.nlm.nih.gov/pmc/articles/PMC5690920/

[12] J. H. Jensen, J. A. Helpern, A. Ramani, H. Lu, and K. Kaczynski, "Diffusional

kurtosis imaging: the quantification of non-gaussian water diffusion by means of magnetic resonance imaging," *Magnetic Resonance in Medicine*, vol. 53, no. 6, pp. 1432–1440, Jun. 2005.

[13] J.-D. Tournier, F. Calamante, and A. Connelly, "Robust determination of the fibre orientation distribution in diffusion MRI: Non-negativity constrained super-resolved spherical deconvolution," *NeuroImage*, vol. 35, no. 4, pp. 1459–1472, May 2007. [Online]. Available: https://www.sciencedirect.com/science/article/pii/S1053811907001243

[14] N. Simard, A. D. Fernback, N. B. Konyer, F. Kerins, and M. D. Noseworthy, "Assessing measurement consistency of a diffusion tensor imaging (DTI) quality control (QC) anisotropy phantom," *Magnetic Resonance Materials in Physics, Biology and Medicine*, Mar. 2025. [Online]. Available: https://doi.org/10.1007/s10334-025-01244-4

[15] E. L. Hahn, "Spin Echoes," *Physical Review*, vol. 80, no. 4, pp. 580–594, Nov. 1950, publisher: American Physical Society. [Online]. Available: https://link.aps.org/doi/10.1103/PhysRev.80.580

[16] H. Y. Carr and E. M. Purcell, "Effects of Diffusion on Free Precession in Nuclear Magnetic Resonance Experiments," *Physical Review*, vol. 94, no. 3, pp. 630–638, May 1954, publisher: American Physical Society. [Online]. Available: https://link.aps.org/doi/10.1103/PhysRev.94.630

[17] H. C. Torrey, "Bloch Equations with Diffusion Terms," *Physical Review*, vol. 104, no. 3, pp. 563–565, Nov. 1956, publisher: American Physical Society. [Online]. Available: https://link.aps.org/doi/10.1103/PhysRev.104.563

[18] D. Le Bihan, E. Breton, D. Lallemand, P. Grenier, E. Cabanis, and M. Laval-Jeantet, "MR imaging of intravoxel incoherent motions: application to diffusion and perfusion in neurologic disorders," *Radiology*, vol. 161, no. 2, pp. 401–407, Nov. 1986.

[19] R. Brown, "A brief account of microscopical observations made in the months of June, July and August 1827 on the particles contained in the pollen of plants; and on the general existence of active molecules in organic and inorganic bodies," *The Philosophical Magazine*, vol. 4, no. 21, pp. 161–173, Sep. 1828. [Online]. Available: https://www.tandfonline.com/doi/full/10.1080/14786442808674769

[20] A. Einstein, "Über die von der molekularkinetischen Theorie der Wärme geforderte Bewegung von in ruhenden Flüssigkeiten suspendierten Teilchen," *Annalen der Physik*, vol. 322, no. 8, pp. 549–560, Jan. 1905. [Online]. Available: https://onlinelibrary.wiley.com/doi/10.1002/andp.19053220806

[21] E. O. Stejskal and J. E. Tanner, "Spin Diffusion Measurements: Spin Echoes in the Presence of a Time-Dependent Field Gradient," *The Journal of Chemical Physics*, vol. 42, no. 1, pp. 288–292, Jan. 1965. [Online]. Available: https://pubs.aip.org/jcp/article/42/1/288/81544/Spin-Diffusion-Measurements-Spin-Echoes-in-the

[22] D. Le Bihan, "Molecular diffusion, tissue microdynamics and microstructure," *NMR in Biomedicine*, vol. 8, no. 7, pp. 375–386, 1995. [Online]. Available: https://onlinelibrary.wiley.com/doi/abs/10.1002/nbm.1940080711

[23] M. E. Moseley, J. Kucharczyk, J. Mintorovitch, Y. Cohen, J. Kurhanewicz, N. Derugin, H. Asgari, and D. Norman, "Diffusion-weighted MR imaging of acute

stroke: correlation with T2-weighted and magnetic susceptibility-enhanced MR imaging in cats," *AJNR. American journal of neuroradiology*, vol. 11, no. 3, pp. 423–429, May 1990.

[24] J. A. Stokum, V. Gerzanich, and J. M. Simard, "Molecular pathophysiology of cerebral edema," *Journal of Cerebral Blood Flow & Metabolism*, vol. 36, no. 3, pp. 513–538, Mar. 2016. [Online]. Available: https://www.ncbi.nlm.nih.gov/pmc/articles/PMC4776312/

[25] S. Warach, J. Gaa, B. Siewert, P. Wielopolski, and R. R. Edelman, "Acute human stroke studied by whole brain echo planar diffusion-weighted magnetic resonance imaging," *Annals of Neurology*, vol. 37, no. 2, pp. 231–241, Feb. 1995.

[26] P. Mansfield, "Multi-planar image formation using NMR spin echoes," *Journal of Physics C: Solid State Physics*, vol. 10, no. 3, p. L55, Feb. 1977. [Online]. Available: https://dx.doi.org/10.1088/0022-3719/10/3/004

[27] J. G. Pipe, V. G. Farthing, and K. P. Forbes, "Multishot diffusion-weighted FSE using PROPELLER MRI," *Magnetic Resonance in Medicine*, vol. 47, no. 1, pp. 42–52, Jan. 2002.

[28] P. J. Basser, J. Mattiello, and D. LeBihan, "MR diffusion tensor spectroscopy and imaging," *Biophysical Journal*, vol. 66, no. 1, pp. 259–267, Jan. 1994.

[29] M. Kubicki, H. Park, C. F. Westin, P. G. Nestor, R. V. Mulkern, S. E. Maier, M. Niznikiewicz, E. E. Connor, J. J. Levitt, M. Frumin, R. Kikinis, F. A. Jolesz, R. W. McCarley, and M. E. Shenton, "DTI and MTR abnormalities in schizophrenia: Analysis of white matter integrity,"

NeuroImage, vol. 26, no. 4, pp. 1109–1118, Jul. 2005. [Online]. Available: https://www.sciencedirect.com/science/article/pii/S1053811905001874

[30] K. Kantarci, M. E. Murray, C. G. Schwarz, R. I. Reid, S. A. Przybelski, T. Lesnick, S. M. Zuk, M. R. Raman, M. L. Senjem, J. L. Gunter, B. F. Boeve, D. S. Knopman, J. E. Parisi, R. C. Petersen, C. R. Jack, and D. W. Dickson, "White-matter integrity on DTI and the pathologic staging of Alzheimer's disease," *Neurobiology of Aging*, vol. 56, pp. 172–179, Aug. 2017. [Online]. Available: https://www.sciencedirect.com/science/article/pii/S0197458017301525

[31] K. J. Painter and T. Hillen, "Mathematical modelling of glioma growth: The use of Diffusion Tensor Imaging (DTI) data to predict the anisotropic pathways of cancer invasion," *Journal of Theoretical Biology*, vol. 323, pp. 25–39, Apr. 2013. [Online]. Available: https://www.sciencedirect.com/science/article/pii/S0022519313000398

[32] G. Raffa, I. Bährend, H. Schneider, K. Faust, A. Germanò, P. Vajkoczy, and T. Picht, "A Novel Technique for Region and Linguistic Specific nTMS-based DTI Fiber Tracking of Language Pathways in Brain Tumor Patients," *Frontiers in Neuroscience*, vol. 10, Dec. 2016, publisher: Frontiers. [Online]. Available: https://www.frontiersin.org/journals/neuroscience/articles/10.3389/fnins.2016.00552/full

[33] J. Reilly, "Eigenvalues, Eigenvectors, and Correlation," in *Fundamentals of Linear Algebra for Signal Processing*. Springer, Cham, 2025, pp. 23–69. [Online]. Available: https://link.springer.com/chapter/10.1007/978-3-031-68915-4_2

[34] P. J. Basser and C. Pierpaoli, "Microstructural and physiological features of tissues elucidated by quantitative-diffusion-tensor MRI," *Journal of Magnetic Resonance. Series B*, vol. 111, no. 3, pp. 209–219, Jun. 1996.

[35] M. Yoshida, M. Hori, K. Yokoyama, I. Fukunaga, M. Suzuki, K. Kamagata, K. Shimoji, A. Nakanishi, N. Hattori, Y. Masutani, and S. Aoki, "Diffusional kurtosis imaging of normal-appearing white matter in multiple sclerosis: preliminary clinical experience," *Japanese Journal of Radiology*, vol. 31, no. 1, pp. 50–55, Jan. 2013. [Online]. Available: https://doi.org/10.1007/s11604-012-0147-7

[36] D. Wu, G. Li, J. Zhang, S. Chang, J. Hu, and Y. Dai, "Characterization of Breast Tumors Using Diffusion Kurtosis Imaging (DKI)," *PLOS ONE*, vol. 9, no. 11, p. e113240, Nov. 2014, publisher: Public Library of Science. [Online]. Available: https://journals.plos.org/plosone/article?id=10.1371/journal.pone.0113240

[37] J. A. Stokum, S. , Chandler, Z. , Jiachen, K. , Robert, S. , Kathirkamanthan, and R. P. Gullapalli, "A longitudinal evaluation of diffusion kurtosis imaging in patients with mild traumatic brain injury," *Brain Injury*, vol. 29, no. 1, pp. 47–57, Jan. 2015, publisher: Taylor & Francis. [Online]. Available: https://doi.org/10.3109/02699052.2014.947628

[38] H. Zheng, J. Lin, Q. Lin, and W. Zheng, "Magnetic Resonance Image of Neonatal Acute Bilirubin Encephalopathy: A Diffusion Kurtosis Imaging Study," *Frontiers in Neurology*, vol. 12, Aug. 2021, publisher: Frontiers. [Online]. Available: https://www.frontiersin.org/journals/neurology/articles/10.3389/fneur.2021.645534/full

[39] J.-X. Cheng, H.-Y. Zhang, Z.-K. Peng, Y. Xu, H. Tang, J.-T. Wu, and J. Xu, "Divergent topological networks in Alzheimer's disease: a diffusion kurtosis imaging analysis," *Translational Neurodegeneration*, vol. 7, no. 1, p. 10, Apr. 2018. [Online]. Available: https://doi.org/10.1186/s40035-018-0115-y

[40] X. Chu, P. Wu, H. Yan, X. Chen, L. Fan, Z. Wu, C. Tao, Y. Ma, Y. Fu, Y. Guo, Y. Dong, C. Yang, and Y. Ge, "Comparison of brain microstructure alterations on diffusion kurtosis imaging among Alzheimer's disease, mild cognitive impairment, and cognitively normal individuals," *Frontiers in Aging Neuroscience*, vol. 14, Aug. 2022, publisher: Frontiers. [Online]. Available: https://www.frontiersin.org/journals/aging-neuroscience/articles/10.3389/fnagi.2022.919143/full

[41] M. Ankele and T. Schultz, "Quantifying microstructure in fiber crossings with diffusional kurtosis." Munich, Germany: Springer International Publishing, Oct. 2015, pp. 150–157. [Online]. Available: https://cg.cs.uni-bonn.de/backend/v1/files/attachments/ankele-miccai15.pdf

[42] G. R. Glenn, J. A. Helpern, A. Tabesh, and J. H. Jensen, "Quantitative Assessment of Diffusional Kurtosis Anisotropy," *NMR in biomedicine*, vol. 28, no. 4, pp. 448–459, Apr. 2015. [Online]. Available: https://www.ncbi.nlm.nih.gov/pmc/articles/PMC4378654/

[43] A. Tabesh, J. H. Jensen, B. A. Ardekani, and J. A. Helpern, "Estimation of tensors and tensor-derived measures in diffusional kurtosis imaging," *Magnetic Resonance in Medicine*, vol. 65, no. 3, pp. 823–836, 2011. [Online]. Available: https://onlinelibrary.wiley.com/doi/abs/10.1002/mrm.22655

[44] J. D. Tournier, F. Calamante, D. G. Gadian, and A. Connelly, "Direct estimation of the fiber orientation density function from diffusion-weighted MRI data using spherical deconvolution," *NeuroImage*, vol. 23, no. 3, pp. 1176–1185, Nov. 2004. [Online]. Available: https://www.sciencedirect.com/science/article/pii/S1053811904004100

[45] Y. D. Reijmer, A. Leemans, S. M. Heringa, I. Wielaard, B. Jeurissen, H. L. Koek, and G. J. Biessels, "Improved Sensitivity to Cerebral White Matter Abnormalities in Alzheimer's Disease with Spherical Deconvolution Based Tractography," *PLOS ONE*, vol. 7, no. 8, p. e44074, Aug. 2012, publisher: Public Library of Science. [Online]. Available: https://journals.plos.org/plosone/article?id=10.1371/journal.pone.0044074

[46] A. M. Auriat, M. R. Borich, N. J. Snow, K. P. Wadden, and L. A. Boyd, "Comparing a diffusion tensor and non-tensor approach to white matter fiber tractography in chronic stroke," *NeuroImage: Clinical*, vol. 7, pp. 771–781, Jan. 2015. [Online]. Available: https://www.sciencedirect.com/science/article/pii/S2213158215000492

[47] Z. Sheng, J. Yu, Z. Chen, Y. Sun, X. Bu, M. Wang, C. Sarica, J. Hernesniemi, B. J. Nelson, A. Zemmar, and J. M. Avecillas-Chasin, "Constrained-Spherical Deconvolution Tractography in the Evaluation of the Corticospinal Tract in Glioma Surgery," *Frontiers in Surgery*, vol. 8, Jul. 2021, publisher: Frontiers. [Online]. Available: https://www.frontiersin.org/journals/surgery/articles/10.3389/fsurg.2021.646465/full

[48] M. Descoteaux, E. Angelino, S. Fitzgibbons, and R. Deriche, "Regularized, fast,

and robust analytical Q-ball imaging," *Magnetic Resonance in Medicine*, vol. 58, no. 3, pp. 497–510, Sep. 2007.

[49] P. C. Hansen, "REGULARIZATION TOOLS: A Matlab package for analysis and solution of discrete ill-posed problems," *Numerical Algorithms*, vol. 6, no. 1, pp. 1–35, Mar. 1994, company: Springer Distributor: Springer Institution: Springer Label: Springer Number: 1 Publisher: Baltzer Science Publishers, Baarn/Kluwer Academic Publishers. [Online]. Available: https://link.springer.com/article/10.1007/BF02149761

[50] J. Cohen-Adad, M. Descoteaux, and L. L. Wald, "Quality assessment of high angular resolution diffusion imaging data using bootstrap on Q-ball reconstruction," *Journal of Magnetic Resonance Imaging*, vol. 33, no. 5, pp. 1194–1208, 2011. [Online]. Available: https://onlinelibrary.wiley.com/doi/abs/10.1002/jmri.22535

[51] E. N. Manson, A. N. Mumuni, I. Shirazu, F. Hasford, S. Inkoom, E. Sosu, M. P. Aikins, and G. A. Mohammed, "Development of a standard phantom for diffusion-weighted magnetic resonance imaging quality control studies: A review," *Polish Journal of Medical Physics and Engineering*, vol. 28, no. 4, pp. 169–179, Nov. 2022. [Online]. Available: https://sciendo.com/article/10.2478/pjmpe-2022-0020

[52] N. Yanasak and J. Allison, "Use of capillaries in the construction of an MRI phantom for the assessment of diffusion tensor imaging: demonstration of performance," *Magnetic Resonance Imaging*, vol. 24, no. 10, pp. 1349–1361,

Dec. 2006. [Online]. Available: https://linkinghub.elsevier.com/retrieve/pii/S0730725X06002396

[53] S. J. Kim, C. G. Choi, J. K. Kim, S.-C. Yun, G.-H. Jahng, H.-K. Jeong, and E. J. Kim, "Effects of MR Parameter Changes on the Quantification of Diffusion Anisotropy and Apparent Diffusion Coefficient in Diffusion Tensor Imaging: Evaluation Using a Diffusional Anisotropic Phantom," *Korean Journal of Radiology*, vol. 16, no. 2, p. 297, 2015. [Online]. Available: https://www.kjronline.org/DOIx.php?id=10.3348/kjr.2015.16.2.297

[54] M. E. Komlosh, D. Benjamini, A. S. Barnett, V. Schram, F. Horkay, A. V. Avram, and P. J. Basser, "Anisotropic phantom to calibrate high-q diffusion MRI methods," *Journal of magnetic resonance (San Diego, Calif. : 1997)*, vol. 275, pp. 19–28, Feb. 2017. [Online]. Available: https://www.ncbi.nlm.nih.gov/pmc/articles/PMC5325680/

[55] V. J. Witherspoon, M. E. Komlosh, D. Benjamini, E. Özarslan, N. Lavrik, and P. J. Basser, "Novel pore size-controlled, susceptibility matched, 3D-printed MRI phantoms," *Magnetic Resonance in Medicine*, vol. 91, no. 6, pp. 2431–2442, Jun. 2024. [Online]. Available: https://onlinelibrary.wiley.com/doi/10.1002/mrm.30029

[56] R. Lorenz, M. E. Bellemann, J. Hennig, and K. A. Il'yasov, "Anisotropic Phantoms for Quantitative Diffusion Tensor Imaging and Fiber-Tracking Validation," *Applied Magnetic Resonance*, vol. 33, no. 4, 2008, publisher: Springer-Verlag. [Online]. Available: https://journals.scholarsportal.info/details/09379347/v33i0004/nfp_apfqdtiafv.xml

[57] P. Pullens, A. Roebroeck, and R. Goebel, "Ground truth hardware phantoms for validation of diffusion-weighted MRI applications," *Journal of Magnetic Resonance Imaging*, vol. 32, no. 2, pp. 482–488, 2010. [Online]. Available: https://onlinelibrary.wiley.com/doi/abs/10.1002/jmri.22243

[58] E. Farrher, J. Kaffanke, A. A. Celik, T. Stöcker, F. Grinberg, and N. J. Shah, "Novel multisection design of anisotropic diffusion phantoms," *Magnetic Resonance Imaging*, vol. 30, no. 4, pp. 518–526, 2012, publisher: Elsevier. [Online]. Available: https://journals.scholarsportal.info/details/0730725x/v30i0004/518_nmdoadp.xml

[59] A. Tachibana, Y. Tachibana, J. Kershaw, H. Sano, M. Fukushi, and T. Obata, "Comparison of Glass Capillary Plates and Polyethylene Fiber Bundles as Phantoms to Assess the Quality of Diffusion Tensor Imaging," *Magnetic Resonance in Medical Sciences*, vol. 17, no. 3, pp. 251–258, 2018.

[60] S. J. Teipel, S. Reuter, B. Stieltjes, J. Acosta-Cabronero, U. Ernemann, A. Fellgiebel, M. Filippi, G. Frisoni, F. Hentschel, F. Jessen, S. Klöppel, T. Meindl, P. J. W. Pouwels, K.-H. Hauenstein, and H. Hampel, "Multicenter stability of diffusion tensor imaging measures: A European clinical and physical phantom study," *Psychiatry Research: Neuroimaging*, vol. 194, no. 3, pp. 363–371, Dec. 2011. [Online]. Available: https://www.sciencedirect.com/science/article/pii/S0925492711002046

[61] U. Hakulinen, A. Brander, P. Ryymin, J. Öhman, S. Soimakallio, M. Helminen, P. Dastidar, and H. Eskola, "Repeatability and variation of region-of-interest

methods using quantitative diffusion tensor MR imaging of the brain," *BMC medical imaging*, vol. 12, p. 30, Oct. 2012.

[62] E. A. Wilde, J. M. Provenzale, B. A. Taylor, M. Boss, A. Zuccolotto, R. Hachey, S. Pathak, D. F. Tate, T. J. Abildskov, and W. Schneider, "Assessment of quantitative magnetic resonance imaging metrics in the brain through the use of a novel phantom," *Brain Injury*, vol. 32, no. 10, pp. 1265–1275, Aug. 2018, publisher: Taylor & Francis. [Online]. Available: https://doi.org/10.1080/02699052.2018.1494855

[63] J. M. Provenzale, B. A. Taylor, E. A. Wilde, M. Boss, and W. Schneider, "Analysis of variability of fractional anisotropy values at 3T using a novel diffusion tensor imaging phantom," *The Neuroradiology Journal*, vol. 31, no. 6, pp. 581–586, Dec. 2018.

[64] E. M. De Souza, E. T. Costa, and G. Castellano, "Investigation of anisotropic fishing line-based phantom as tool in quality control of diffusion tensor imaging," *Radiological Physics and Technology*, vol. 12, no. 2, pp. 161–171, Jun. 2019. [Online]. Available: http://link.springer.com/10.1007/s12194-019-00507-9

[65] M. Kimura, H. Yabuuchi, R. Matsumoto, K. Kobayashi, Y. Yamashita, K. Nagatomo, R. Mikayama, T. Kamitani, K. Sagiyama, and Y. Yamasaki, "The reproducibility of measurements using a standardization phantom for the evaluation of fractional anisotropy (FA) derived from diffusion tensor imaging (DTI)," *Magnetic Resonance Materials in Physics, Biology and Medicine*, vol. 33, no. 2, pp. 293–298, Apr. 2020. [Online]. Available: http://link.springer.com/10.1007/s10334-019-00776-w

[66] L. W. Kasa, R. A. M. Haast, T. K. Kuehn, F. N. Mushtaha, C. A. Baron, T. Peters, and A. R. Khan, "Evaluating High Spatial Resolution Diffusion Kurtosis Imaging at 3T: Reproducibility and Quality of Fit," *Journal of magnetic resonance imaging: JMRI*, vol. 53, no. 4, pp. 1175–1187, Apr. 2021.

[67] F. N. Mushtaha, T. K. Kuehn, O. El-Deeb, S. A. Rohani, L. W. Helpard, J. Moore, H. Ladak, A. Moehring, C. A. Baron, and A. R. Khan, "Design and characterization of a 3D-printed axon-mimetic phantom for diffusion MRI," *Magnetic Resonance in Medicine*, vol. 86, no. 5, pp. 2482–2496, 2021, publisher: Wiley. [Online]. Available: https://journals.scholarsportal.info/details/07403194/v86i0005/2482_dacoa3apfdm.xml

[68] S. D. Walter, M. Eliasziw, and A. Donner, "Sample size and optimal designs for reliability studies," *Statistics in Medicine*, vol. 17, no. 1, pp. 101–110, 1998. [Online]. Available: https://onlinelibrary.wiley.com/doi/abs/10.1002/%28SICI%291097-0258%2819980115%2917%3A1%3C101%3A%3AAID-SIM727%3E3.0.CO%3B2-E

[69] M. Grech-Sollars, P. W. Hales, K. Miyazaki, F. Raschke, D. Rodriguez, M. Wilson, S. K. Gill, T. Banks, D. E. Saunders, J. D. Clayden, M. N. Gwilliam, T. R. Barrick, P. S. Morgan, N. P. Davies, J. Rossiter, D. P. Auer, R. Grundy, M. O. Leach, F. A. Howe, A. C. Peet, and C. A. Clark, "Multi-centre reproducibility of diffusion MRI parameters for clinical sequences in the brain," *NMR in Biomedicine*, vol. 28, no. 4, pp. 468–485, Apr. 2015. [Online]. Available: https://onlinelibrary.wiley.com/doi/10.1002/nbm.3269